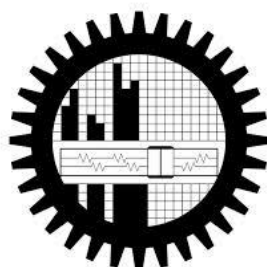


FABRICATION OF HIGH QUALITY MULTIFERROIC BiFeO₃ BASED THIN FILMS USING COST-EFFECTIVE PROCESSING ROUTE

BY
Hasan Muhammad Usama
STUDENT NUMBER 1015112020
August, 2018

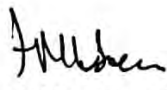
THIS THESIS PAPER IS SUBMITTED TO THE DEPARTMENT OF MATERIALS AND METALLURGICAL
ENGINEERING IN PARTIAL FULFILLMENT OF THE REQUIREMENTS FOR THE DEGREE OF MASTER
OF SCIENCE IN MATERIALS AND METALLURGICAL ENGINEERING



DEPARTMENT OF MATERIALS AND METALLURGICAL ENGINEERING
BANGLADESH UNIVERSITY OF ENGINEERING AND TECHNOLOGY

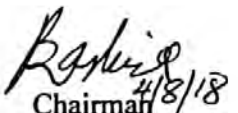
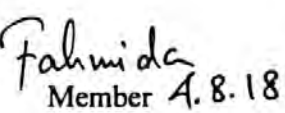
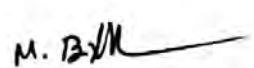
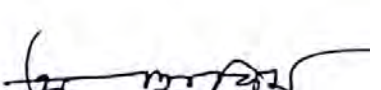
CANDIDATES' DECLARATION

IT IS DECLARED HEREBY THAT THIS THESIS PAPER OR ANY PART OF IT HAS NOT BEEN
SUBMITTED ANYWHERE ELSE FOR THE AWARD OF ANY DEGREE

.....

Hasan Muhammad Usama
B.Sc. Engg., MME, BUET

The thesis titled “Fabrication of High Quality Multiferroic BiFeO₃ Based Thin Films Using Cost-Effective Processing Route” submitted by Hasan Muhammad Usama, Student No. 1015112020, Session October 2015 has been accepted as satisfactory in partial fulfillment of the requirements for the degree of Master of Science in Materials and Metallurgical Engineering on August 4, 2018.

BOARD OF EXAMINERS

- | | | |
|--|--------------|--|
| (i) Dr. A. K. M. Bazlur Rashid | (Supervisor) | 
Chairman 4/8/18 |
| Professor, Department of MME | | |
| BUET, Dhaka-1000 | | |
| (ii) Dr. Fahmida Gulshan | (Ex-Officio) | 
Member A. 8. 18 |
| Professor and Head, Department of MME | | |
| BUET, Dhaka-1000 | | |
| (iii) Dr. Kazi. Md. Shorowordi | | 
Member |
| Professor, Department of MME | | |
| BUET, Dhaka-1000 | | |
| (iv) Dr. Md. Muktadir Billah | | 
Member |
| Assistant Professor, Department of MME | | |
| BUET, Dhaka-1000 | | |
| (v) Dr. M. A. Hakim | | 
Member (External) |
| Individual Consultant, Department of GCE | | |
| BUET, Dhaka-1000 | | |

ACKNOWLEDGEMENTS

First and foremost, I would like to thank the Almighty for blessing me with the means and opportunity to carry out this thesis work successfully and in due time in spite of difficulties.

I express my sincere gratitude to my supervisor, Prof. Dr. A.K.M Bazlur Rashid for his kind supervision, indispensable guidance, valuable and constructive suggestions, liberal help and encouragement during this thesis work. I especially appreciate his procurement of the spin coater without which this thesis would not have been possible. I would also like to thank him endlessly for acceding to my unfair demands of reviewing and correcting this thesis in a very short amount of time.

I thank Dr. Fahmida Gulshan, Professor and Head, Department of Materials and Metallurgical Engineering, BUET, for arranging my thesis defense in a very short time despite all her busyness. I am also grateful for the support she has provided and, I believe, will continue to provide me with.

I profoundly thank Mr. Muhammad Shahriar Bashar, Senior Scientific Officer, IFRD, BCSIR for being so kind and allowing me access to various equipment throughout my work, and for the support and advice he continues to give me, without which the research work would have become unduly lengthened.

I am equally grateful to Dr. Md. Abdul Matin, Head, Department of Glass and Ceramic Engineering, BUET, for giving me permission to use the XRD, SEM and UV-Vis spectrometer in an accessible way. Without the lab facilities provided, this research would not have been possible.

I pay my gratitude to Dr. Md. Abdullah Zubair, Assistant Professor, Department of Glass and Ceramic Engineering and Dr. Ahmed Sharif, Professor, Department of Materials and Metallurgical Engineering for their constant help, support, motivation and encouragement in conducting this thesis.

I would like to thank Dr. Md. Abu Hashan Bhuiyan, Professor, Department of Physics, BUET for allowing me to use the electrometers available in his lab and for offering from his vast pool of knowledge regarding thin films. The same gratitude also goes to Dr. Mohammad Jellur Rahman, Assistant Professor, Department of Physics, BUET.

I am also thankful to Mr. Shahjalal Rana and Mr. Najmul Hossain, Department of Glass and Ceramic Engineering, BUET, for their promptness and help in testing my SEM and XRD samples. Without them going out of their way to assist me, this project would never have been complete on time.

My examiners also deserve my heartfelt gratitude for agreeing to hold my thesis defense within an unreasonably short period of time. Thank you Dr. Md. Abdul Hakim, Dr. Kazi Md. Shorowordi and Dr. Md. Muktadir Billah!

Finally, I would like to thank my parents immensely for supporting me throughout the years and believing in me. I would also like to thank my wife for bearing with my untimely busyness and making compromises for my sake.

ABSTRACT

Spin coated thin films of bismuth ferrite (BiFeO_3) were produced using cost effective sol-gel processing route. Precursor solutions were made using $\text{Bi}(\text{NO}_3)_3 \cdot 5\text{H}_2\text{O}$ and $\text{Fe}(\text{NO}_3)_3 \cdot 9\text{H}_2\text{O}$ as the metal sources in a 2-methoxyethanol solvent. Acetic acid was used as the chelating agent. The solution was dispensed on a preheated soda-lime glass or FTO-coated glass substrate and spun in a spin coater to obtain the thin films. The selection of annealing temperature was revealed to be an important aspect since low annealing temperatures such as 450°C was found to be insufficient for producing phase pure bismuth ferrite. Increasing the annealing temperature had a beneficial effect on phase formation as well as microstructure development. Annealing at 550°C for 30 mins was enough to produce phase pure bismuth ferrite and well crystallized films with low variation in grain size. A pronounced effect of substrate preheating was observed on the film topography and continuity. Increasing the substrate preheat temperature from 30°C to 70°C produced increasingly continuous and smooth thin films. Some degree of preferred orientation or texture was induced by rapid heating of the dried films. Annealing a thin seed layer first, before subsequent coatings were deposited on top of the seed layer, improved the texture and phase purity of the rapidly heated films. On the other hand, Bi non-stoichiometry of 5% seemed to change the microstructure along with the unit cell size. The presence of different types of defects in these Bi-deficient or Bi-excess films were argued to be the main reason behind the observed changes. Interestingly, Bi-deficiency was found to be beneficial for producing a less porous microstructure with a slightly larger grain size. Electrical measurements could not be made reliably due to the presence of excessive dust in the films. Dust was reduced appreciably by filtration of the solution but measurements were still unreliable, indicating the unsuitability of the working environment for producing high quality thin films. Magnetic properties of the films were evaluated and weak ferromagnetism of bismuth ferrite was confirmed. The magnetization seemed to be the highest in the Bi-excess film, owing to its many vacancies in the Fe sub-lattice. Optical properties of the films were measured and the band gap ($\sim 2.73\text{ eV}$) was revealed to be unaffected by Bi non-stoichiometry

Table of Contents

CANDIDATES' DECLARATION	Error! Bookmark not defined.
ACKNOWLEDGEMENTS.....	iv
ABSTRACT.....	v
List of Figures	ix
List of Tables	xii
CHAPTER 1 : INTRODUCTION	1
1.1 Multiferroics and Bismuth Ferrite	1
1.2 Thin films of Bismuth Ferrite	2
1.3 Aim of the Current Work.....	3
CHAPTER 2 : LITERATURE REVIEW	4
2.1 Primary Ferroics.....	4
2.1.1 Ferroelectric materials	7
2.1.2 Materials with magnetic order	10
2.1.3 Ferroelastic material.....	13
2.2 Multiferroics	13
2.2.1 Classification of multiferroics.....	14
2.3 Bismuth Ferrite	15
2.3.1 History of BiFeO ₃	16
2.3.2 Crystal structure of BiFeO ₃	17
2.3.3 Phase diagram of BiFeO ₃	20

2.3.4 Ferroelectric properties of BiFeO ₃	21
2.3.5 Magnetic order of BiFeO ₃	22
2.3.6 Applications of BiFeO ₃	24
2.4 BiFeO ₃ Thin Films.....	27
2.4.1 Sol-gel Process.....	28
2.4.2 CSD-derived BFO thin films	31
CHAPTER 3 : EXPERIMENTAL.....	37
3.1 Precursor Solution Preparation	37
3.2 Substrate Cleaning:	38
3.3 Film Deposition:	38
3.3.1 Solution dispensation	38
3.3.2 Spinning and heating schedule.....	39
3.4 Film Characterization:	40
3.4.1 Topography and microstructure	40
3.4.2 Phase analysis	41
3.4.3 Electrical characterization.....	41
3.4.4 Magnetic and optical characterization	44
CHAPTER 4 : RESULTS AND DISCUSSIONS	45
4.1 Role of Dispensing Method:	45
4.2 Film Topography and Structure:	46
4.2.1 Effect of preheating.....	46

4.2.2	Role of solvent ratio.....	52
4.2.3	Effect of annealing temperature.....	54
4.2.4	Effect of heating rate.....	57
4.2.5	Effect of Bi non-stoichiometry	58
4.2.6	Effect of seed layer	61
4.2.7	Effect of substrate	63
4.3	Electrical Characterization:.....	64
4.3.1	MIM configuration.....	64
4.3.2	Planar electrode configuration	67
4.3.3	Four-point probe measurement.....	67
4.4	Magnetic Properties:	67
4.5	Optical Properties:	70
	CONCLUSIONS.....	74
	SUGGESTIONS FOR FUTURE WORK.....	76
	BIBLIOGRAPHY.....	77

List of Figures

Fig. 2.1. From left to right: hysteresis loops of ferromagnetic, ferroelectric and ferroelastic materials.....	6
Fig. 2.2. Schematic representation of ferroelectric and ferromagnetic characteristics.....	6
Fig. 2.3. Perovskite crystal structure showing a dipole moment generated by a displaced B-site atom.....	9
Fig. 2.4. Elementary cell of BaTiO ₃ in the ‘up’ and ‘down’ spontaneous polarization states..	9
Fig. 2.5. Schematic potential energy of a ferroelectric material.....	10
Fig. 2.6. Common examples of magnetic dipole ordering, from ref. [3].....	12
Fig. 2.7. Multiferroics materials are those that present more than one ferroic order	14
Fig. 2.8. Schematic illustration of a structural transition process (a) ideal cubic structure Pm-3m without tilting ($a^0a^0a^0$) ; (b) R-3c structure tilted along three axes with the same angle ($a^-a^-a^-$) ; (c) Displacement of Bi ion towards [111] direction based on R3c.....	18
Fig. 2.9. Crystal structure of bismuth ferrite (a) in the hexagonal setting, (b) in the hexagonal setting with the distorted perovskite sub-structure shown, and (c) viewed along the c-axis... 19	
Fig. 2.10. Phase diagram of Fe ₂ O ₃ and Bi ₂ O ₃	20
Fig. 2.11. Schematic of crystal structure of BFO and ferroelectric polarization (arrow).....	21
Fig. 2.12. Schematic showing different types of magnetic ordering – the last three are types of antiferromagnetism	22
Fig. 2.13. Spin canting due to anti-symmetric exchange.....	23
Fig. 2.14. Schematics of the 64 nm antiferromagnetic spin cycloid.....	23
Fig. 2.15. Preparation of various structures via the sol-gel approach.....	29
Fig. 2.16. Diagram of the free energies of a sol-gel derived amorphous film [13]	35
Fig. 3.1. A typical dark brown precursor solution.....	37
Fig. 3.2. A typical 3 layer film after annealing.....	40

Fig. 3.3. (a) Gold electrodes sputtered on top for MIM structure and (b) planar configuration of electrodes. Two wires were attached using silver paste	42
Fig. 3.4. Four point probe setup.....	44
Fig. 4.1. Incomplete coverage of the substrate in static dispense.....	45
Fig. 4.2. Film appearance after drying using different preheat temperatures (a) 30° C, (b) 40° C, (c) 50° C, (d) 60° C and (e) 70° C.....	46
Fig. 4.3. Optical micrograph of dried film deposited using 30° C preheat at magnification (a) 200x and (b) 1000x	47
Fig. 4.4. Optical micrographs of dried films deposited using preheat temperatures of (a) 40° C, (b) 50° C, (c) 60° C and (d) 70° C at 1000x magnification	48
Fig. 4.5. Optical micrographs of dried film deposited using 50° C preheat showing (a) the central clear area and (b) the whitish peripheral area at 1000x magnification	49
Fig. 4.6. Optical micrograph of annealed film deposited using 30° C preheat at 1000x magnification	49
Fig. 4.7. SEM images of annealed films deposited using (a) 30° C and (b) 70° C preheat	50
Fig. 4.8. XRD pattern of annealed films deposited using preheat temperatures of 30° C, 50° C and 70° C; peaks labeled according to hexagonal unit cell	51
Fig. 4.9. XRD patterns of films deposited using precursor solutions with 2-MOE:acetic acid ratio of 2:1, 3:1 and 4:1; peaks labeled according to hexagonal unit cell.....	53
Fig. 4.10. SEM images of films deposited using precursor solutions with solvent ratio of (a) 2:1, (b) 3:1 and (c) 4:1	53
Fig. 4.11. (a) XRD patterns of films annealed at 450° C, 500° C and 550° C; '*' denotes peaks not belonging to BFO. (b) Magnified portion of the patterns from $2\theta=22^\circ$ - 23° showing shifting of the (012) _h /(100) _{pc} peak; peaks labeled according to hexagonal unit cell	55
Fig. 4.12. SEM images of films annealed at (a) 450° C, (b) 500° C and (c) 550° C.....	56

Fig. 4.13. Optical micrograph of central region of rapidly heated film at 500x magnification	57
Fig. 4.14. Effect of heating rate on the XRD pattern; Bi:Fe ratio and annealing temperature were kept same.....	58
Fig. 4.15. (a) XRD patterns of S1, S2 and S3 annealed at 550° C; (b) Magnified portion of the patterns from 2θ=22°- 23° showing shifting of the (012) _h /(100) _{pc} peak.....	59
Fig. 4.16. SEM images of (a) S1, (b) S2 and (c) S3 annealed at 550° C.....	60
Fig. 4.17. Cross-sectional SEM images of (a) seed layer and (b) usual 3 layer film	61
Fig. 4.18. XRD patterns of seeded and normal films heated at different rates.....	62
Fig. 4.19. (a) SEM image and (b) XRD pattern of BFO deposited on FTO coated glass substrate; '*' denotes peaks belonging to FTO.....	64
Fig. 4.20. Optical micrographs of films deposited using (a, b) unfiltered solution and (c, d) filtered solution	65
Fig. 4.21. Raw M-H curves of empty sample holder and S2 annealed at 450° C, 500° C and 550° C	68
Fig. 4.22. Extracted M-H curves of films	70
Fig. 4.23. Optical absorbance of the thin films.....	71
Fig. 4.24. $(\alpha.hv)^2$ vs. hv plots for S1, S2 and S3 annealed at 550° C	72

List of Tables

Table 2.1. Crystalline classes in relation to ferroelectrics.....	8
--	---

CHAPTER 1 : INTRODUCTION

1.1 Multiferroics and Bismuth Ferrite

Multiferroic materials are those materials which display more than one primary ferroic order in the same phase. This class of material is fascinating both from a technological perspective, and from a fundamental physics point of view due to its rare combination of properties. Most interest has been directed towards multiferroics in which electric and magnetic ordering exists. These often show a coupling between the electric and magnetic order parameters; they are magnetoelectrics.

Bismuth ferrite (BiFeO_3 ; BFO), a prototypical multiferroic, is the most intensely studied multiferroic material in recent years because it exhibits electric and magnetic ordering up to significantly high temperatures. Its ferroelectric transition point or Curie temperature is ~ 1103 K, and its antiferromagnetic Neel temperature is ~ 640 K [1, 2]. Its structure has been described as a rhombohedrally distorted perovskite structure belonging to the space group R3c [2]. If imagined as an ideal perovskite unit cell the Bi^{3+} atoms take the corner positions, while the O^{2-} ions make up the octahedral cage inside of which sits the Fe^{3+} ion. The rhombohedral distortion amounts to rotating the oxygen octahedron along the pseudo-cubic [111] direction, with adjacent octahedron having a rotation of the opposite sense, and off centering of the Bi^{3+} ions resulting in a non-centrosymmetric structure essential for ferroelectricity.

The magnetic structure is of the G-type antiferromagnetic type. It means that, each Fe^{3+} ion is surrounded by six other Fe^{3+} ions of the opposite spin. Simply stated this results in the Fe^{3+} ions in the hexagonal (001) planes being ordered ferromagnetically with adjacent planes being coupled antiferromagnetically. The spins aren't exactly anti-parallel; the small canting of the spins would have given rise to weak ferromagnetism, but the presence of a spin cycloid masks such a possibility. The cycloid consists of Fe^{3+} ion spins being rotated slightly in going from

one ion to the next along the $[110]_h$ direction completing a full period after 64 nm, thus making the cycloid incommensurate with the crystal lattice [3].

Most of the research done on BFO aims to improve its phase purity, reduce its leakage current and/or increase its magnetization [4-6]. Recently, BFO has been proven to hold promise as a novel photovoltaic and photocatalytic material too [7], and hence its optical properties have also been studied extensively.

1.2 Thin films of Bismuth Ferrite

Almost all of BFO's potential uses require it to be in high quality thin film architecture [8, 9]. For example, epitaxial BFO thin films are needed to attain the maximum polarization possible and open the doors for its use as a ferroelectric material [10]. BFO's promising photovoltaic performance utilizing the anomalous photovoltaic effect (or bulk photovoltaic effect) can only be harnessed in high quality thin film form too [11]. For optimum properties the phase purity, microstructure, topography etc. of the thin films are of paramount importance.

Producing the highest quality films require quite expensive experimental setup and raw materials. Deposition techniques such as Molecular Beam Epitaxy (MBE), Pulsed Laser Deposition (PLD) or other methods falling under Physical Vapor Deposition (PVD) processes, are very costly to setup and maintain. Moreover, getting epitaxial, or at least textured, films involve expensive single crystal substrates [10-12].

On the other hand, Chemical Solution Deposition (CSD) is a cheap and easy method of thin film fabrication. Specific processes falling under CSD include dip coating, spray pyrolysis, spin coating etc [13]. The equipment necessary for CSD processes are generally not that expensive and raw materials are cost effective as well. Many researchers have produced polycrystalline BFO films successfully by CSD [7, 14-17], but in most cases the properties cannot be compared with their single crystalline or highly textured counterparts synthesized by

more expensive processes. Moreover, inducing texture in the films and/or increasing the grain size seems to be a challenge in CSD processes, especially when non-single crystal substrates such as glass are used. Hence, we believe there is still room for improvement and more work to be done in understanding how to produce quality BFO thin films by CSD.

1.3 Aim of the Current Work

The aim of the present undertaking, stated in brief, is to synthesize BFO thin films via spin coating with an emphasis on minimizing the associated costs and assess its various properties thereafter. More specifically, the main focuses of this work are:

- a) Producing BFO thin films with dense microstructure, enhanced phase purity and maximal substrate coverage using simple and easily available raw materials as well as substrates
- b) Investigating the effect of numerous process variables on the structure, phase composition and topography of the thin films
- c) Narrowing down the region in parameter space that gives the best overall films
- d) Exploring the possibility of inducing texture in the films
- e) Characterizing the films' electrical, magnetic and optical properties

Although there is much literature available describing and documenting the production of BFO thin films using spin coating, one still has to face a lot of practical challenges when attempting to reproduce published work. This is because, a scientific paper captures only the most essential aspects of a work and can quite easily neglect details that are deemed dispensable in maintaining the cogency, coherency and brevity of the article. But many times, these details turn out to be quite important from a practical stand point. Since, to the best of our knowledge, no work has been done in producing any kind of BFO thin film in Bangladesh, these "details" had to be learnt or found out by first-hand experimentation.

CHAPTER 2 : LITERATURE REVIEW

2.1 Primary Ferroics

A primary ferroic material exhibits a spontaneous magnetization, a spontaneous polarization or a spontaneous strain, and these spontaneous orderings can be reoriented by an external magnetic field, electric field, or mechanical stress below a characteristic temperature (Curie temperature). There are four primary ferroic order parameters. They are described below.

- **Ferroelectricity:** It is the property due to which materials show spontaneous, stable polarization that can be switched hysteretically by an applied electric field; antiferroelectric materials have ordered anti-parallel dipole moments which cancel each other completely within each crystallographic unit cell resulting in net zero polarization [18]. E.g. BaTiO₃ (ferroelectric).
- **Ferromagnetism:** It is the property due to which materials exhibit spontaneous, stable magnetization that can be switched hysteretically by an applied magnetic field; antiferromagnetic materials possess ordered anti-parallel magnetic moments which nullify each other completely within each magnetic unit cell resulting in net zero magnetization [18]. E.g. Fe₃O₄ (ferromagnetic).
- **Ferroelasticity:** Materials display a spontaneous, stable deformation which if applied upon by a stress, can be switched hysteretically [18]. E.g Au_xCu_{1-x}Zn.
- **Ferrotoroidicity:** Materials possess a stable and spontaneous order parameter that is taken to be the curl of a magnetization or polarization. By analogy with the above examples, it is anticipated that this order parameter may be switchable. Ferrotoroidic materials have evaded unambiguous observation.

Ferro- is a prefix which means iron in Latin; it is primitively used to describe materials exhibiting strong magnetic properties as iron does. Apart from iron, other elements like cobalt, nickel and rare earth elements also exhibit magnetic behavior called ferromagnetism, which enables materials made from the above-mentioned elements to form permanent magnets. Ferromagnetic materials were reported to have a long-range ordering phenomenon at the atomic level. Many small domains can be found in a magnetic material with plenty of unpaired electrons inside. Microscopically, those unpaired electrons are not randomly aligned; they interact with others to make the alignment in the same direction within the same domain. However, these domains are randomly aligned so that on the whole, they cancel out to make the macroscopic magnetization zero. When an external magnetic field is applied, those domains whose magnetic moment is aligned with the external magnetic field grow at the expense of their neighboring domains, causing materials to be magnetized. This phenomenon is characterized by a hysteresis loop of magnetization M as a function of external magnetic field H , as illustrated in Fig. 2.1. It is obvious that the magnetization is saturated at high magnetic field and a remnant magnetization can still exist in the absence of the field. In addition, the direction of magnetization could be reversed provided that the external magnetic field is switched oppositely with quite strong field intensity.

However, the ferromagnetic material can lose its ferromagnetic properties under thermal agitation, the temperature that characterizes this phenomenon is known as the “Curie temperature (T_c)”, above which spontaneous ferromagnetic ordering is broken and paramagnetism takes its place. The material now has a small, positive susceptibility to magnetic fields and can't keep this magnetization after removal of the external field. When such a material is cooled down and crosses the Curie temperature, it undergoes a phase transition from a non-ferroic to ferroic state. These transitions are generally accompanied with a lowering of the crystal symmetry.

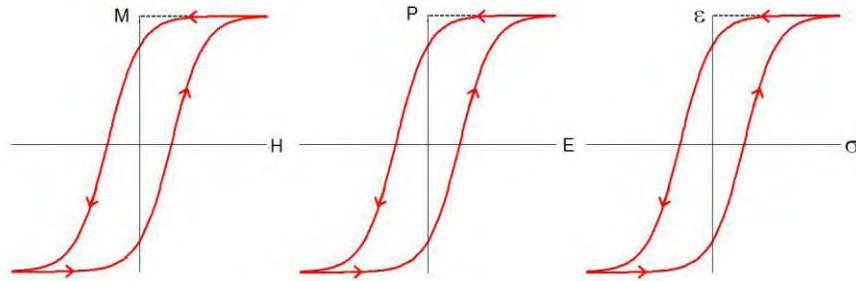


Fig. 2.1. From left to right: hysteresis loops of ferromagnetic, ferroelectric and ferroelastic materials

For example bulk BaTiO₃ an archetypal ferroelectric presents a transition from a cubic paraelectric structure to a tetragonal ferroelectric structure around 120°C [19].

Ferroelectricity and ferroelasticity are analogous to ferromagnetism. Polarization and strain are induced by externally applied electric field and mechanical stress respectively. They both show hysteresis loops with spontaneous electric polarization and strain, as depicted in Fig. 2.1. Fig. 2.2 shows how ferroelectrics and ferromagnetics permit the orientations of electrical polarization and magnetization to be reversed by applying an electric field and magnetic field, respectively.

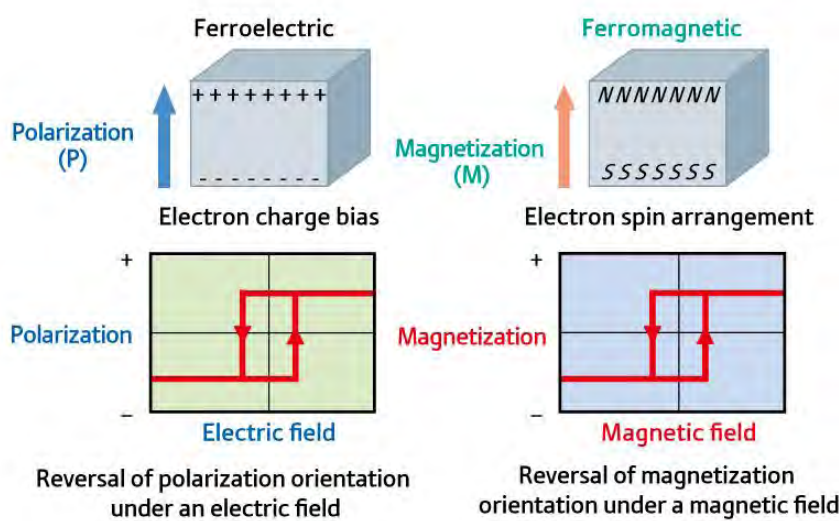


Fig. 2.2. Schematic representation of ferroelectric and ferromagnetic characteristics.

Actually, the discovery of ferroelectricity dates back to the early 20th century when ferromagnetism had already been discovered. Since the appearance of hysteresis loops from ferroelectricity and ferromagnetism look quite similar, the prefix ferro- was carried forward to describe ferroelectricity, though many ferroelectric materials have nothing to do with iron.

2.1.1 Ferroelectric materials

For the past few decades, ferroelectric materials have received a great amount of interests because of their various uses in many applications such as nonvolatile ferroelectric random access memories (NVFRAM), dynamic random access memories, sensors and micro actuators [18].

A crystal is said to be ferroelectric when it possesses at least two equilibrium orientations of the spontaneous polarization vector in the absence of an external electric field, and the spontaneous polarization can be switched between those orientations by an electric field. The polar character of the orientation states should represent an absolutely stable configuration in a null field [20].

Among the thirty-two crystal classes, eleven of them are characterized by the existence of a center of symmetry. The remaining twenty-one crystal classes do not have a center of symmetry. Thus, it is possible for the 21 groups to (i) have one or more polar axes, and (ii) possess odd-rank tensor properties. The only exception is the group 432, which lacks a center of symmetry, but has other symmetry operations that destroy polarity. All non-centrosymmetric point groups exhibit piezoelectric effect that is defined by a change in electric polarity under applied stress, and vice versa. Out of the twenty piezoelectric classes, ten possess a unique polar axis, the spontaneous polarization of which depends on temperature. This is called the pyroelectric effect. Ferroelectric crystals belong to the pyroelectric family, which in

addition has a spontaneous polarization that can be reversed by external electric field, i.e. more than one equivalent direction for P_s [21]. This classification is shown succinctly in Table 2.1.

A (proper) ferroelectric possesses a spontaneous polarization of the electric dipole which can be switched by the application of an electric field. This polarization is due to a lack of inversion symmetry within the crystal structure. For example, consider the most extensively studied and widely used classic perovskite of the form ABO_3 , in which a central positive B-ion (a transition metal element) is surrounded by an octahedron of negatively charged oxygen ions (Fig. 2.3). A shift in the position of the B-site ion would break the inversion symmetry and cause the induction of a dipole moment, giving rise to ferroelectric order. Such shifts can occur during

Table 2.1. Crystalline classes in relation to ferroelectrics

32 crystalline classes			
21 classes non-centrosymmetric			
20 classes piezoelectric			
10 classes pyroelectric	non pyroelectric	non piezoelectric	centrosymmetric
ferroelectric	non ferroelectric		
e.g. : BaTiO_3 , PbTiO_3	e.g. : Tourmaline	e.g. : Quartz	

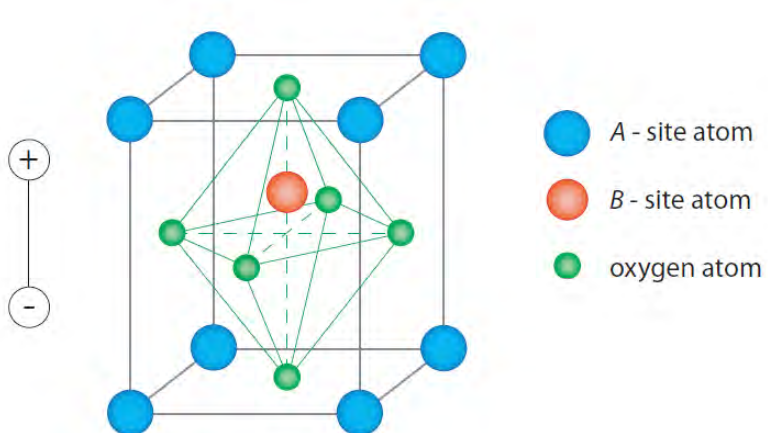


Fig. 2.3. Perovskite crystal structure showing a dipole moment generated by a displaced B-site atom

structural phase transitions, in which the system moves from a high to low symmetry state (e.g. cubic to tetragonal). One of the best known examples of a proper ferroelectric is BaTiO_3 . In reference to Fig. 2.3, the Ba^{2+} cations are located at the corners of the unit cell (A-site). A dipole moment occurs due to relative displacements of the Ti^{4+} (B-site) and O^{2-} ions from their symmetrical positions. A sufficiently large external electric field can cause the displacement to ‘switch’ (Fig. 2.4) thus reversing the polarization direction, in fulfillment of a primary condition of ferroelectricity. In these sorts of ferroelectrics the center ion usually has a ‘double well’ potential energy curve. As shown in Fig. 2.5, this is what makes the polarization spontaneous, as the lowest energy state is the one with the ion displaced.

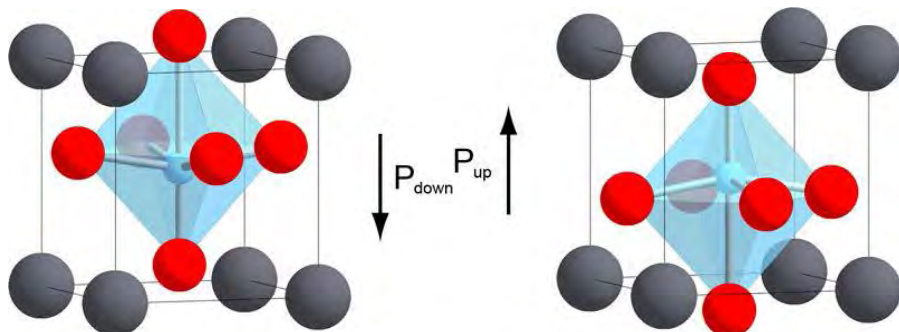


Fig. 2.4. Elementary cell of BaTiO_3 in the ‘up’ and ‘down’ spontaneous polarization states

In the majority of ferroelectric perovskites, the B-site atom has an empty d electron shell, which allows covalent bonding with the full p orbital of the oxygen atoms. Ferroelectricity can also occur due to the existence of lone pairs of electrons on the outer shell of the A-site atom, which are highly susceptible to polarization. This is the cause of ferroelectricity in BiFeO_3 .

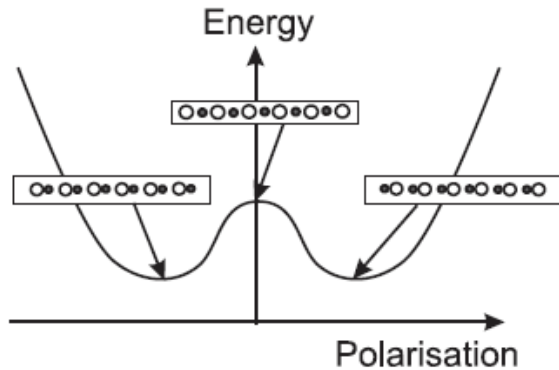


Fig. 2.5. Schematic potential energy of a ferroelectric material

In an improper ferroelectric, the spontaneous polarization is not due to a polar displacement of the ions, but occurs as a result of some other effect within the material. In a geometric ferroelectric, the dipole moment occurs due to non-polar lattice distortions, due to e.g. electrostatic forces rather than changes in chemical bonding. An example of this is in YMnO_3 , where a ferroelectric state is due to a buckling of the rigid MnO_5 bipyramids. In charge ordered ferroelectrics, the spontaneous polarization is dependent on electron correlations in the material. Such charge ordered ferroelectricity is observed in LuFe_2O_4 . Improper ferroelectricity can also occur due to magnetic order.

2.1.2 Materials with magnetic order

The phenomenon of magnetism has been known to mankind for many thousands of years. Lodestone (Fe_3O_4) was the first permanent magnetic material to be identified and studied. The magnetic moment of an atom/ion has three principal sources: (1) the spin of electrons; (2) electron orbital angular momentum about the nucleus; and (3) a change in the orbital moment

induced by an applied magnetic field. The first two effects give paramagnetic contributions to the magnetization, and the third gives a diamagnetic contribution [22].

In a crystal, the overall magnetic property depends on two factors: (i) the magnetic response associated with each atom/ion, and (ii) the interactions between these magnetic moments. In the case that there are no unpaired electrons around each atom/ion, there will be no net magnetic moment associated with them, bearing in mind that both orbital moments and electron spins cancel to zero in a fully filled orbital. This material will show diamagnetic behavior; the orbital and spin magnetic moments will oppose the external magnetic field, just as a conducting loop of wire opposes a changing magnetic flux by inducing its own oppositely oriented magnetic field (Lenz's law). When there are unpaired electrons, every atom/ion has a net magnetic moment. Depending on the interactions between the magnetic dipoles, the material may show (i) paramagnetism (PM); (ii) ferromagnetism (FM); (iii) antiferromagnetism (AFM) and (iv) ferrimagnetism (FIM). In a paramagnetic material, alignment of adjacent moments is not observed due to thermal fluctuations being stronger than any driving force which might align the moments.

Ferromagnetism, anti-ferromagnetism and ferrimagnetism are all manifestations of the same quantum mechanical interaction; exchange interaction [22]. This interaction is purely quantum mechanical with no classical analogue. It has connections with Pauli's exclusion principle. Basically, according to Pauli's exclusion principle two electrons cannot occupy the same state without having different spin magnetic moments. An implication of this is, since oppositely aligned spins can occupy the same state they can be much closer to each other on average. This would increase the coulombic forces between them and thus make the system energy higher. Consequently parallel spins stay further away from each other and their net coulombic energy is lower, which is a very simplified account of the origin of ferromagnetism.

In some cases, the overall energy might be lowered if spins are aligned anti-parallel. Such ordering gives rise to anti-ferromagnetism with a net zero magnetization. Ferrimagnetic order consists of anti-parallel unequal moments, resulting in a non-zero net magnetization.

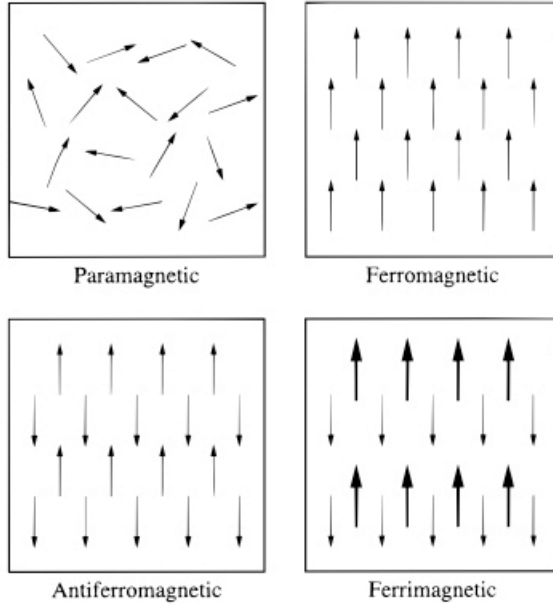


Fig. 2.6. Common examples of magnetic dipole ordering, from ref. [3]

Ferromagnetism is a very strong magnetic response compared with paramagnetic and diamagnetic behaviors. It is characterized by a transition temperature (Neel temperature, T_N). Above this temperature, the material is paramagnetic. Below this temperature, it is ferromagnetic. The magnetic susceptibility, $\chi = M/H$, which defines the degree of magnetization of a material in response to a magnetic field, is a good indication of their magnetic properties. If χ is positive the material is paramagnetic, and the magnetic field is strengthened by the presence of the material. If χ is negative then the material is diamagnetic and the magnetic field is weakened in the presence of the material. The magnetic susceptibility of a ferromagnetic substance is not linear and much larger than unity [23]. Different types of magnetic ordering are schematically shown in Fig. 2.6.

2.1.3 Ferroelastic material

Ferroelastic materials develop a spontaneous strain below a phase transition temperature. From the symmetry point of view, the material undergoes a structural phase transition from a high symmetry phase to a low symmetry phase, which is characterized by a ‘broken symmetry’ of the high symmetry phase [24].

The phase transition mechanism results in a spontaneous strain. The spontaneous strain can be quite large. For example, the spontaneous strain of a typical ferroelastic material is >2%. The correlated changes in the enthalpy of the crystal related to this formation of spontaneous strain often reach some 6 KJ/mole, an energy which would be equivalent to changes in thermochemical phase diagrams of some hundreds of degrees in temperature. In order to release the energy created by the phase transition, a twin domain structure is often created within a ferroelastic crystal, where the dominant twin planes are oriented approximately perpendicular to each other.

2.2 Multiferroics

Multiferroic materials are single-component materials or composites exhibiting two or more ferroic properties such as ferromagnetism, ferroelectricity, or ferroelasticity, as shown in Fig. 2.7.

In a broader definition, it also covers materials with ferro- and antiferro- orders. There are significant scientific and technological interests in these materials due to their unusual responses, including very large magneto-electric susceptibility, giant magnetostriction, and energy coupling coefficients [4, 25]. In addition, the ability to couple between the spontaneous order parameters offers extra degrees of freedom in the design of conventional devices. Examples of single component multiferroics are BiFeO_3 (an anti-ferromagnetic/ferroelectric perovskite), and Fe-Ga (a ferromagnetic/ferroelastic alloy). The ability to combine magnetic

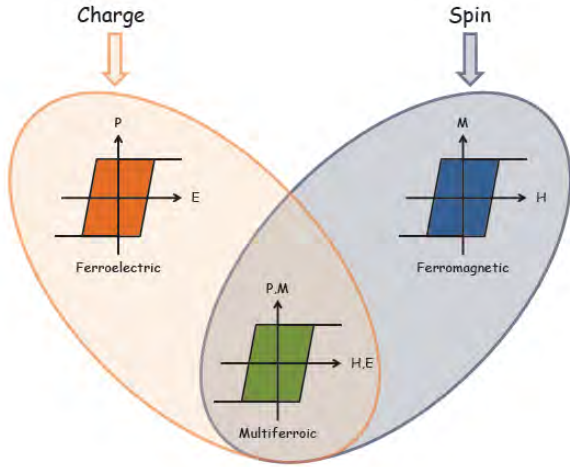


Fig. 2.7. Multiferroics materials are those that present more than one ferroic order

and ferroelectric properties within one material and the potential functionality that can be achieved has resulted in much of the early work on multiferroics being concentrated within magnetic ferroelectrics [26]. Combining these two properties has, however, proven to be difficult. Normally, these two order parameters are mutually exclusive; yet a number of materials have simultaneously presented magnetic and ferroelectric properties. Coupling of the parameters within the multiferroic system tends to be weak. The microscopic mechanisms of magnetism and ferroelectricity are very different from each other therefore do not strongly interfere [27].

2.2.1 Classification of multiferroics

The microscopic origin of magnetism is basically the same in all magnets: it is the presence of localized electrons, mostly in the partially filled d or f shells of transition-metal or rare-earth ions, which have a corresponding spin, or magnetic moment. Exchange interactions between the localized moments lead to magnetic order. The situation with ferroelectrics is quite different. There are several different microscopic sources of ferroelectricity, and accordingly one can have different types of multiferroics.

Broadly, multiferroics can be classified as single-phase or composite multiferroics. Generally speaking, there are two groups of multiferroics. Single-phase multiferroics are those materials that show both ferroelectric and ferromagnetic order in the same phase [25, 28]. Thus multiferroicity is intrinsic to the material. The scarcity of single phase multiferroic materials makes composite materials an interesting alternative. As opposed to single-phase multiferroics, multiferroic order is not intrinsic but results from the combination of two materials that are ferroelectric and ferromagnetic, separately. Therefore, the availability of ferromagnetic and ferroelectric materials at room temperature makes it somewhat easy, to obtain multiferroic composite materials at room temperature.

Single-phase multiferroics can be further classified into two groups. The first group, called type-I multiferroics, contains those materials in which ferroelectricity and magnetism have different sources and appear largely independently of one another, though there is some coupling between them. In these materials, ferroelectricity typically appears at higher temperatures than magnetism, and the spontaneous polarization P is often rather large (of the order $10\text{-}100 \mu\text{C}/\text{cm}^2$). Examples are BiFeO_3 ($T_{\text{FE}} \sim 1100\text{K}$, $T_{\text{N}} = 643 \text{ K}$, $P \sim 90\mu\text{C}/\text{cm}^2$) and YMnO_3 ($T_{\text{FE}} \sim 914\text{K}$, $T_{\text{N}} = 76 \text{ K}$, $P \sim 6\mu\text{C}/\text{cm}^2$). The second group, which we can call type-II multiferroics, is the relatively recently discovered materials [8, 25], in which magnetism causes ferroelectricity, implying a strong coupling between the two. However, the polarization in these materials is usually much smaller ($10^{-2}\mu\text{C}/\text{cm}^2$). Many groups are also investigating composite multiferroics that consist of known magnets and ferroelectrics in the form of multilayers and self-organized nanostructures [28].

2.3 Bismuth Ferrite

Bismuth ferrite (BFO) is one of the most interesting members of the multiferroic family which shows both ferroelectric and antiferromagnetic properties in a single phase at room

temperature. It is one of the few multiferroics that has Curie and Neel temperatures far above room temperature. It shows magnetoelectric coupling at room temperature and such coupling is strongly enhanced by proper doping.

2.3.1 History of BiFeO₃

The basic idea that crystals could be simultaneously ferromagnetic and ferroelectric probably originated with Pierre Curie in the 19th century [29]. After switching was discovered in ferroelectric Rochelle Salt by Valasek in 1920 [30] there was a rash of supposed discoveries of magnetoelectric properties by Perrier, but unfortunately in materials such as Ni in which they are now understood to be impossible. A history of this period of solid-state physics is given in O’ Dell’s text [31].

True magnetoelectricity—defined as a linear term in the free energy was first understood theoretically by Dzyaloshinskii [32] with special predictions being made for Cr₂O₃ and discovered experimentally in that material by Astrov [33]. However this material is paraelectric and antiferromagnetic, making microelectronics applications impractical.

The more interesting case of ferromagnetic ferroelectrics waited for some years until the work of Schmid on boracites [34]. The boracites are also impractical materials for device applications: they have low symmetry with large unit cells and grow in needle shapes; more importantly, they exhibit magnetoelectricity only at extremely low temperatures. Meanwhile Smolenskii’s group in Leningrad pioneered [4] the study of bismuth ferrite, BiFeO₃, but they found that they could not grow single crystals and that ceramic specimens were too highly conducting (probably caused by oxygen vacancies and mixed Fe valences) to be used in applications [4]. They tried to address the conductivity problem by doping other ions into both the A and B sites of the lattice.

Reviews of the general study of magnetoelectricity appeared by Schmid in 1994 [35] and more recently by Fiebig [28] and by Eerenstein et al. [25]. The current interest in bismuth ferrite was stimulated primarily by a 2003 paper from Ramesh's group [10], which showed that it had unexpectedly large remnant polarization. At any rate, the 2003 Science paper has proved enormously stimulating, and has inspired both new fundamental physics and exciting device applications. Increasing efforts have now been devoted to the research focusing on the preparation and characterization of BiFeO_3 in forms of film, bulk and nanostructure.

2.3.2 Crystal structure of BiFeO_3

The room-temperature phase of BiFeO_3 is classed as rhombohedral (space group R3c) [2]. The perovskite-type unit cell has a lattice parameter, a_{pc} , of 3.965\AA and a rhombohedral angle, α_{pc} , of $89.3\text{--}89^\circ$ at room temperature [36] with ferroelectric polarization along $[111]_{\text{pseudocubic}}$ [37].

A very important structural parameter is the rotation angle of the oxygen octahedra. This angle would be 0° for a cubic perovskite with perfectly matched ionic sizes. A measure of how well the ions fit into a perovskite unit cell is the ratio $(r_{\text{Bi}} + r_{\text{O}})/l$, where r is the ionic radius of the respective ion and l is the length of the octahedral edge. This is completely analogous to the commonly used Goldschmid tolerance factor [36], which is defined as $t = (r_{\text{Bi}} + r_{\text{O}})/(r_{\text{Fe}} + r_{\text{O}})$. For BiFeO_3 we obtain $t=0.88$ using the ionic radii of Shannon [38], with Bi^{3+} in eightfold coordination (the value for 12-fold coordination is not reported) and Fe^{3+} in sixfold coordination and high spin. When this ratio is smaller than one, the oxygen octahedra must buckle in order to fit into a cell that is too small. For BiFeO_3 , ω is ca. $11\text{--}14^\circ$ around the polar $[111]$ axis [36]. The displacement of the A-site bismuth cation (shown in Fig. 2.8) along the $[111]$ axis brings about a non-centrosymmetric polarization resulting in the ferroelectric property.

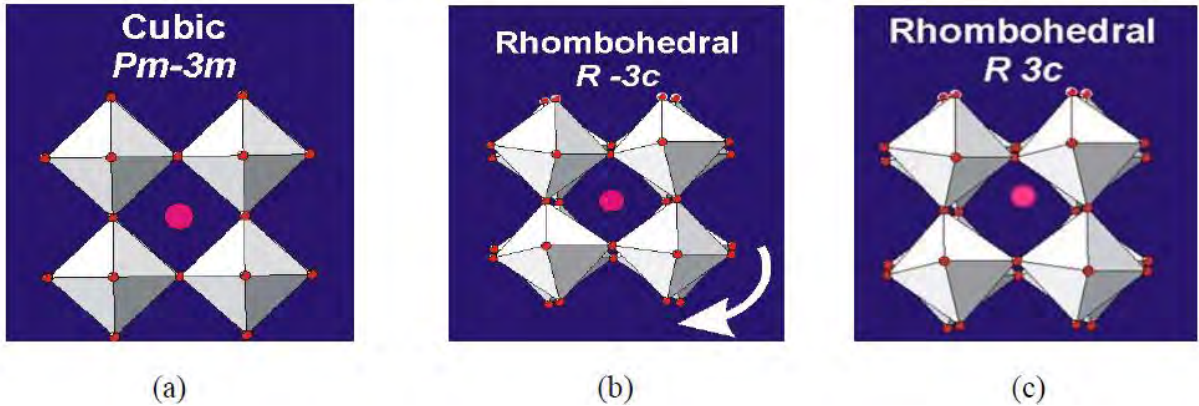


Fig. 2.8. Schematic illustration of a structural transition process (a) ideal cubic structure Pm-3m without tilting ($a^0a^0a^0$) ; (b) R-3c structure tilted along three axes with the same angle ($a^-a^-a^-$) ; (c) Displacement of Bi ion towards [111] direction based on R3c.

The lattice parameter and crystal structure of BiFeO_3 are dependent on the temperature. It was well documented that, except for the long Bi-Fe bond distance, the lattice parameter a , c , the volume of unit cell, the short bond distance of Bi-Fe as well as the bond angles gradually increase with increase in temperature. As a consequence of these variations, magnetism and polarization are reported to be gradually reduced, and structural phase transitions are also induced from the rhombohedrally distorted R3c perovskite structure to an orthorhombic Pnma structure and eventually to a cubic structure.

The unit cell can also be described in a hexagonal frame of reference, with the hexagonal c -axis parallel to the diagonals of the perovskite cube, i.e., $[001]_{\text{hexagonal}} \parallel [111]_{\text{pseudocubic}}$. The hexagonal lattice parameters are $a_{\text{hex}} = 5.58\text{\AA}^\circ$ and $c_{\text{hex}} = 13.90\text{\AA}^\circ$ [2]. The structure is shown in Fig. 2.9.

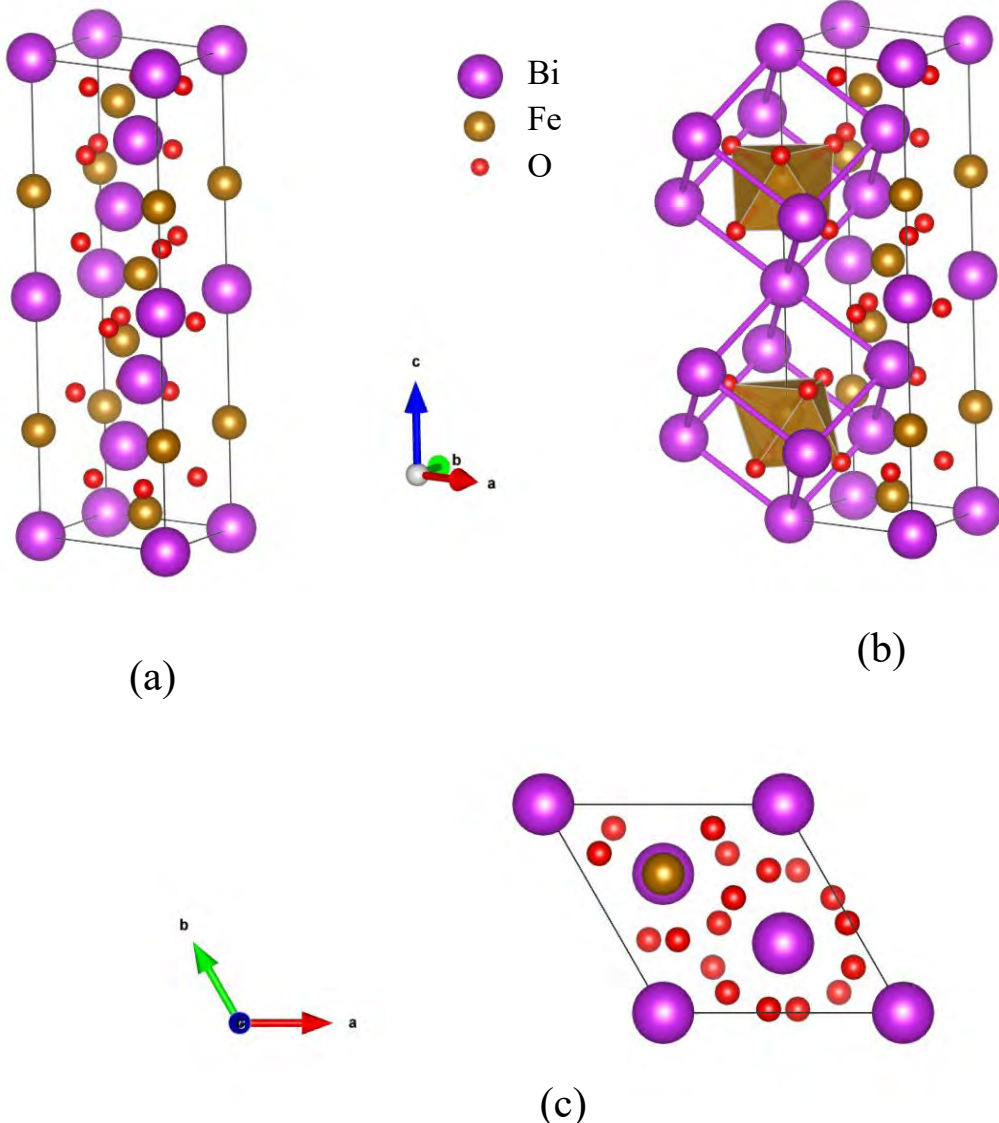


Fig. 2.9. Crystal structure of bismuth ferrite (a) in the hexagonal setting, (b) in the hexagonal setting with the distorted perovskite sub-structure shown, and (c) viewed along the c-axis

In the figure, the displacement of the Bi²⁺ ions along the [001] direction can be easily seen. The Fe³⁺ ion sitting between two Bi²⁺ ions is not in the middle in Fig. 2.9(a). The distortion of the oxygen octahedra can also be visualized in context with the pseudo-cubic perovskite setting. The bottom octahedron is rotated along the [001] axis in relation to the top octahedron, Fig. 2.9(b). In Fig. 2.9(c) the three-fold symmetry of the structure due to the 3-fold axes running perpendicular to the page is shown.

2.3.3 Phase diagram of BiFeO₃

The phase diagram of Fe₂O₃ and Bi₂O₃ is presented below in Fig. 2.10, unequal amount of Fe₂O₃ and Bi₂O₃ is seen to bring about impurity phases Bi₂₅FeO₄₀ (bismuth-rich) and Bi₂Fe₄O₉ (bismuth-deficient). BiFeO₃ is usually prepared from equal parts of Bi₂O₃ and Fe₂O₃, and under high temperatures it can decompose back into these starting materials, as shown in Eq. 2.1.

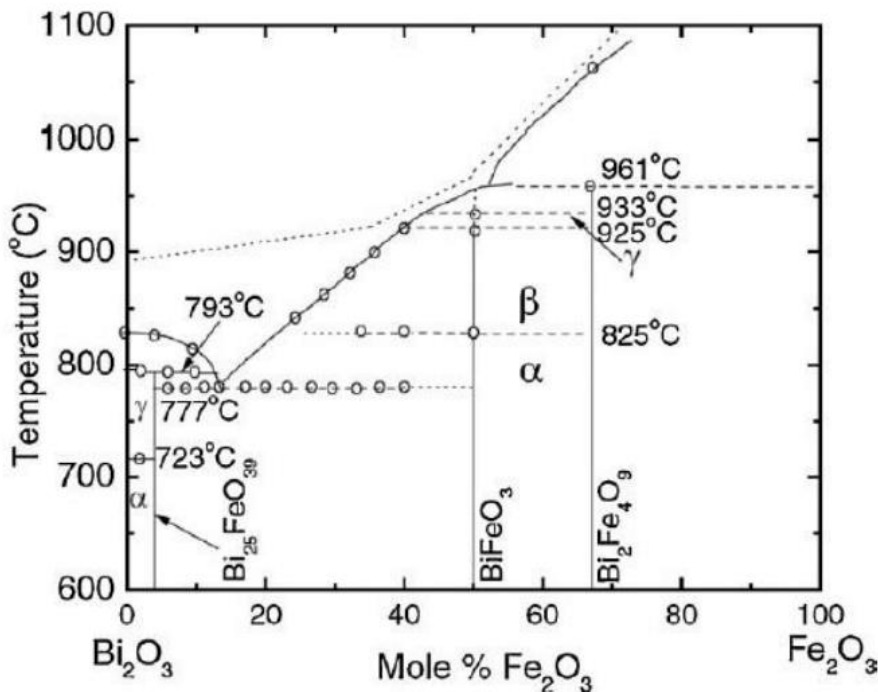


Fig. 2.10. Phase diagram of Fe₂O₃ and Bi₂O₃

At approximately 825° C there is a first-order transition to a high-temperature β phase that is accompanied by a sudden volume contraction [39, 40]. The transition is also accompanied by a peak in the dielectric constant [40]; this has been taken as an indication of a ferroelectric–paraelectric transition, although dielectric peaks can also occur in ferroelectric–ferroelectric transitions, such as the orthorhombic–rhombohedral transition in the archetypal perovskite ferroelectric BaTiO₃ (which is also first order). Nevertheless, although there is disagreement about the exact symmetry of the β phase above 825°C, most reports agree that it is

centrosymmetric [41-43], so it is probably a safe bet that the α - β transition at $T_C = 825^\circ \text{ C}$ is indeed the ferroelectric–paraelectric transition.

2.3.4 Ferroelectric properties of BiFeO_3

The ferroelectric state arises from a large displacement of the Bi ions relative to the FeO_6 octahedra in BiFeO_3 as shown in Fig. 2.11. The ferroelectric polarization lies along the pseudocubic $\langle 111 \rangle$ leading to the formation of eight possible polarization variants, corresponding to four structural variants [44].

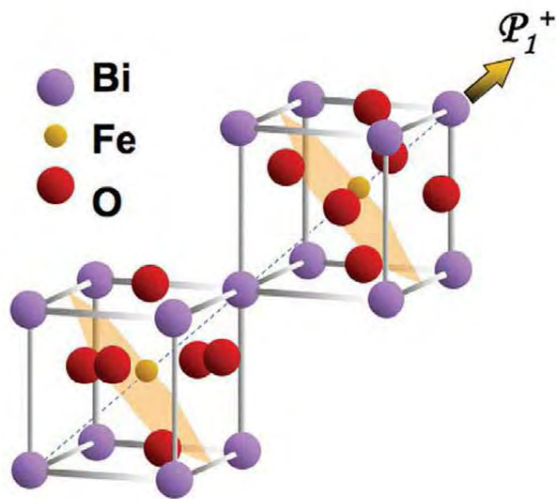


Fig. 2.11. Schematic of crystal structure of BFO and ferroelectric polarization (arrow)

Electrical characterization on bulk BiFeO_3 has been very difficult due to the low resistivity of samples. The controversy about whether it is ferroelectric or antiferroelectric was finally settled based on the hysteresis loop measured by Teague et al. [45]. They performed the experiment in liquid nitrogen, which lowered the charge carrier density and mobility, and in turn lowered the leakage current. The measured spontaneous polarization was $3.5 \mu\text{C}/\text{cm}^2$ along the $\langle 100 \rangle$ direction, which represents $6.1 \mu\text{C}/\text{cm}^2$ in the $\langle 111 \rangle$ direction. This value is much smaller than what would be expected for a ferroelectric material with such high Curie temperature and large

distortion. The leakage problem, likely due to defects and non-stoichiometry, has been hampering more comprehensive studies about the bulk BiFeO₃ and has limited applications of this material. To overcome this problem, recent work has focused on reducing leakage current using proper dopants or other methods.

2.3.5 Magnetic order of BiFeO₃

The local short range magnetic ordering of BFO is G-type antiferromagnetic: each Fe³⁺ spin is surround by six antiparallel spins on the nearest Fe neighbors (Fig. 2.12). The anti-parallel alignment is a result of the super-exchange (or Kramers–Anderson supereexchange) interaction [46], which is the strong (usually) antiferromagnetic coupling between two next-to-nearest neighbor cations through a non-magnetic anion. In this way, it differs from direct exchange in which there is coupling between nearest neighbor cations not involving an intermediary anion.

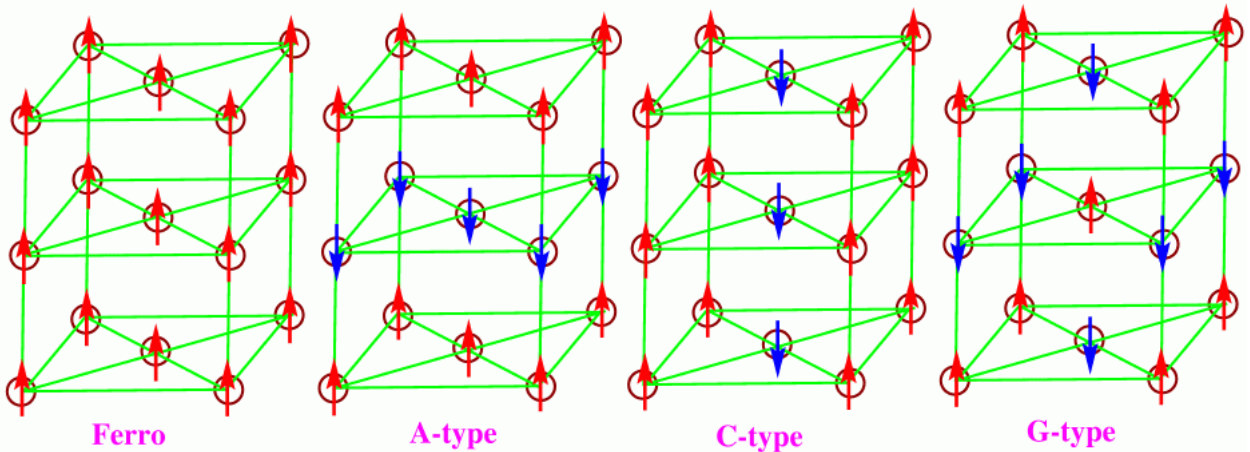


Fig. 2.12. Schematic showing different types of magnetic ordering – the last three are types of antiferromagnetism

Unlike a perfect antiferromagnet, however, the spins are not exactly anti-parallel to each other. There is a small canting angle, a slight tilt in each of the spins away from perfect co-linearity. Spin canting is due to two factors contrasting each other: isotropic exchange would align the spins exactly anti-parallel, while antisymmetric exchange arising from relativistic effects (spin-

orbit coupling) would align the spins at 90° to each other[47]. The net result, as shown in Fig. 2.13, is a small perturbation, the extent of which depends on the relative strength of these effects.

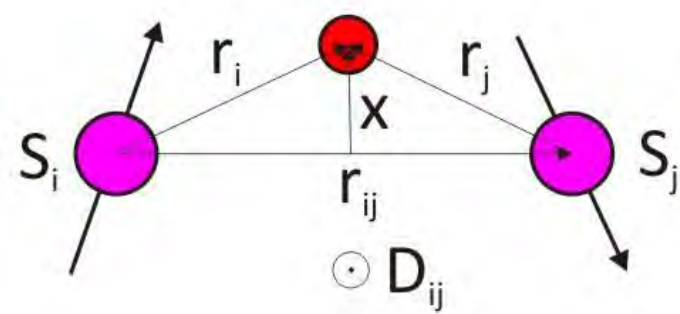


Fig. 2.13. Spin canting due to anti-symmetric exchange

On top of the canted anti-ferromagnetic ordering there is a spatial modulation of the spins. The spin ordering is not homogeneous but is superimposed by an incommensurate cycloid structure with a wavelength of ~ 64 nm along $<10-1>$ _{pseudo-cubic}, as is shown in Fig. 2.14 [3]. The spin rotation plane can also be determined because the magnetic scattering amplitude, in case of neutron diffraction, depends on the component of magnetic moments perpendicular to the scattering vector [48]. The magnetic Néel temperature is about 643 K and the cycloid could be distorted at low temperatures [49].

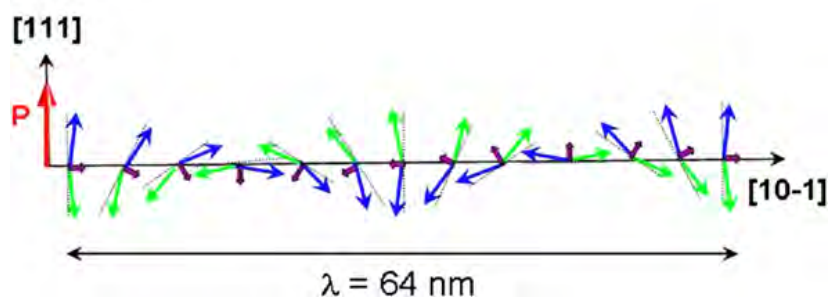


Fig. 2.14. Schematics of the 64 nm antiferromagnetic spin cycloid

2.3.6 Applications of BiFeO₃

Ferroelectric and Piezoelectric Devices

In 2003, Wang et al. [10] reported robust multiferroic behavior in epitaxial BFO thin films which gave rise to a surge of research effort in this material. They showed high quality BFO(001) thin films can possess a high remanent polarization (P_r) up to 55 $\mu\text{C}/\text{cm}^2$ and a piezoelectric coefficient d_{33} of approximately 70 pm/V [10]. An even higher polarization magnitude of $\sim 100 \mu\text{C}/\text{cm}^2$ was demonstrated in BFO (111) thin films due to the (111)-oriented spontaneous polarization direction [50-52]. To put this into context, this is the biggest switchable polarization of any perovskite ferroelectric, and is roughly twice as big as the polarization of the most widely used material in ferroelectric memories, PZT. Moreover, unlike PZT, BiFeO₃ is a lead-free material, a bonus regarding health and safety. For such applications to ever come into fruition, however, important obstacles must be removed, such as:

- a) the higher conductivity (and thus also dielectric losses) of BiFeO₃ relative to PZT,
- b) its tendency to fatigue [53], and
- c) the fact that it appears to thermally decompose at voltages quite close to the coercive voltage [54].

A second potential application unrelated to magnetoelectric properties is piezoelectricity. The piezoelectric coefficient of pure BiFeO₃ is actually quite small. However, its rhombohedral ground state means that mixing it with a tetragonal ferroelectric such as PbTiO₃ leads to a morphotropic phase boundary (MPB) at a composition of 30% mol PbTiO₃ [55].

This is important because MPBs are commonly thought to be the key behind the large piezoelectric coefficients of PZT and relaxors [56], so the MPB of BiFeO₃-PT might lead to equally large piezoelectric constants.

Spintronics

The real drivers behind most of the applied research on BiFeO₃ are magnetoelectric and spintronic applications [57]. Chief among these would be memories that can be written using a voltage and read using a magnetic field. Using a voltage for writing has three advantages:

- a) this can be implemented in a solid-state circuit without mobile parts,
- b) it has a low-energy requirement, and
- c) the voltage requirements automatically scale down with thickness.

Reading the memory magnetically, on the other hand, has the advantage that it is a non-destructive readout process, unlike direct ferroelectric reading, which requires switching the polarization in order to read it. For such memories to actually work, the magnetic state therefore must be, a) electrically switchable and b) magnetically readable.

The first condition is met by BiFeO₃, because the easy plane of its antiferromagnetic domains is correlated with the polar direction, and rotating the ferroelectric polarization results in a rotation of the sub lattice magnetization [48, 58, 59], i.e., the magnetic state of the sample can be changed by a voltage. On the other hand, the second condition is not directly met, because antiferromagnetic (or, at best, weakly canted antiferromagnetic) domains cannot be easily read.

A second line of work uses BiFeO₃ as a barrier layer in spintronics. Sandwiching BiFeO₃ between two ferromagnetic metals results in tunneling magnetoresistance [57, 60]. For this, the only requirement is that the BiFeO₃ layer be reasonably insulating down to tunneling thicknesses. However, an extra ingredient provided by BiFeO₃ is the fact that it also remains a robust and switchable ferroelectric down to a thickness of 2 nm [61], and thus it could in principle be used as an electrically switchable tunnel junction, whereby the ferroelectric state

controls the magnetic state of the thin ferromagnetic electrodes, thus modifying the tunneling magnetoresistance.

Photovoltaics

Ferroelectric materials have been recently reported as one of the promising candidates for photovoltaic materials [14, 62]. Several typical types of ferroelectric oxide perovskites have been extensively investigated for their photovoltaic effects, such as LiNbO₃ [63], BaTiO₃ [19], Pb(Zr,Ti)O₃ [64], and BFO [62, 65]. Among them, the typical oxide ferroelectric perovskites (i.e., LNO, BTO, and PZT) exhibit a gap of more than 3 eV. In comparison, the band gap of BFO is ~2.2 eV for single crystal [62] and 2.7 eV for thin films because of the presence of partially filled d orbitals in Fe³⁺ [66].

To achieve high-efficiency photovoltaic effects, ferroelectrics with small band gap, robust polarization and good dc conductivity, such as BFO, are of general interest. Many parameters of ferroelectric and electrode materials can affect the photovoltaic output, including crystallographic orientations [67], band gap [68, 69], electrical conductivity [70], remnant polarization [71], domain walls[65], microstructure [72] etc. With these understandings, some attempts have been made to enhance the photovoltaic efficiency of BFO-based devices. The overall photovoltaic efficiencies have been improved significantly over the past several years. For example, by modifying the Fe/Cr cationic ordering and engineering the domain size, a band gap as low as 1.5 eV was achieved in Bi₂FeCrO₆ (BFCO) double perovskites [11]. Hence, the BFCO double perovskites could exhibit an unprecedented photovoltaic efficiency of 8.1%. Fan et al. recently reported a giant energy conversion efficiency of up to 0.33% under blue monochromatic illumination in a metal/semiconductor/ferroelectric/metal heterostructure of In₂O₃-SnO₂/ZnO/BiFeO₃/Pt [73].

Besides the tremendous efforts made to enhance the photovoltaic efficiency, the origins of photovoltaic effects in BFO and other ferroelectrics have also attracted a lot of research enthusiasm. So far, various origins have been proposed, such as the bulk photovoltaic effect [74], depolarization field driven photovoltaic effect [75], Schottky barriers [12], and domain wall theory [65]. However, there are still a lot of disputes and controversy on the photovoltaic origins and they deserve further studies undoubtedly.

2.4 BiFeO₃ Thin Films

As mentioned before, owing to the highly desirable properties and rapid advances in physically-derived films, obtaining chemically-derived BFO thin films (in particular via CSD) with properties comparable to PVD BFO remains a challenge. The typical difficulties associated with CSD in obtaining BFO thin films with robust ferroelectric properties include high leakage current [76-78], the formation of secondary phases [78, 79], porous microstructures [80] or crystallographic defects [76]. None of these issues is really unsolvable. MOCVD-derived BFO thin films (i.e. films prepared via an alternate chemical deposition technique) have already been reported, having good ferroelectric properties with square loops, high remnant polarization, and robust d^{33} values [81]. Nevertheless, demonstration of CSD derived epitaxial BFO thin films having high ferroelectric polarization or resistive switching at room-temperature has been rather elusive [82-84]. Until recently, the best properties of CSD-derived BFO thin films had been reported by the Nakamura et al. [85, 86]. In a series of articles they detailed phase development of polycrystalline BFO films with good P-E loops and low leakage current. Much of their discussion in terms of the frequency behavior and electric field dependence was limited to measurements performed at 80 K. It was only recently that the key to obtaining high quality CSD BFO thin films was understood, through a detailed investigation of what happens during gelation [15]. It was shown that for the BFO CSD process, the central underpinning factor is the control of the gelation process such that it yields defect-free gel

films. The paper shed key insight into the chemical processes during gelation (heating). In particular, the delicate competition between solvent evaporation and precursor gelation was ultimately found to be the key that determines if a homogenous gel is achieved. Controlling this balance to yield homogenous gel films was demonstrated as mandatory in order to achieve epitaxial and phase-pure BFO thin films with robust ferroelectric properties [15].

Since CSD derived thin films are based on the sol-gel processing route we will give an overview of it first. Then we will cover the processing of CSD derived BFO thin films.

2.4.1 Sol-gel Process

The sol-gel process is one of the most common and earliest-known chemical synthesis methods for metal oxides that can be traced back to the mid-1800s. In the 1990s the sol-gel process received a major boost for the preparation of multicomponent metal oxides such as perovskite materials [87, 88]. Today sol-gel processes are routinely used to prepare 0-D, 1-D and 2-D perovskite materials. Chemical solution deposition (CSD) is a typical chemical deposition method for thin film preparation using the sol-gel solution as the deposition precursor. It is important to consider the fundamental difference in phase formation pathways for thin film processes, such as PLD compared with CSD. In a typical PLD process, the deposition of the precursor (often of the same stoichiometry as the end material) and the high-temperature crystallization occur nearly simultaneously. In contrast, for CSD the deposition of the precursor solution onto a suitable substrate and the subsequent gelation (drying) process take place at low temperature ($<100^{\circ}\text{C}$) prior to a high-temperature crystallization step [80]. Consequently the formation of a homogenous and defect-free gel film is the first critical step, with complete bearing on the final thin-film microstructure, phase composition and ferroic properties. This key difference must also be viewed as an opportunity – it uniquely allows one to tailor the microstructure before crystallization takes place [80]. The intrinsic low energy of the system

also results in good uniformity. Finally, we reiterate that it is also relatively an economically more viable method of mass fabrication [89].

Regardless of the desired material structure, the fabrication process often starts from a chemical solution, which acts as the precursor. The typical precursor includes a metal source, a solvent and chelation agent. Under appropriate heating conditions, the precursor solution transforms into a cross-linked polymeric state [80], called the “gel”. Due to the liquid nature of the precursor, the end-product material can be fabricated in a range of morphologies simply by “casting” the precursor into an appropriate template or by using different deposition approaches. For example, whilst spin-coating is suitable for thin films, pouring into template is employed for nanowires or nanotubes, and electrospinning is used for nanofibers etc. This is graphically shown in Fig. 2.15.

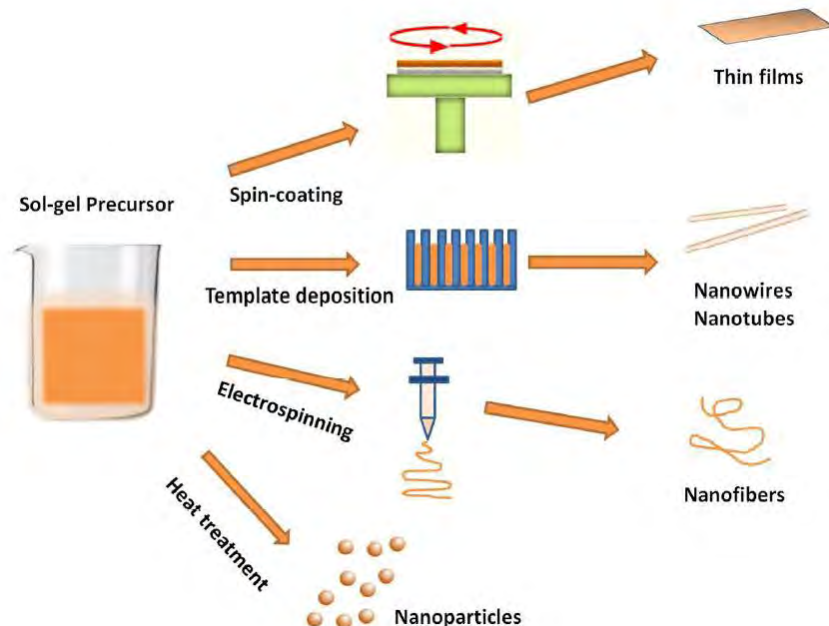


Fig. 2.15. Preparation of various structures via the sol-gel approach

It becomes evident that the chemistry and stoichiometry of the precursor has strong influence on the ultimate quality. Again bearing in mind that phase crystallization occurs during the final

annealing step, it is not commonly possible to identify and thus redress deficiencies that may stem from a poor or inappropriate precursor. It follows therefore that understanding what happens to the precursor at each processing step, and how its stoichiometry and physical features are affected, is of prime importance. In the following, we discuss the main chemical ingredients of a sol-gel precursor used for perovskite metal oxides with a particular emphasis on BFO.

2.4.1.1 Metal compounds

In the traditional sol-gel process, aqueous precursors based on metal alkoxides in water are used as the starting materials, which follow a route of hydrolysis-condensation-gelation [80]. However, metal alkoxides are expensive and thus compromise the economic advantage of the CSD method. Instead, precursor derived from metal salts (metal nitrates or metal chloride) and organic solvent (2-methoxyethanol (2-MOE) [90, 91] or ethylene glycol [92]) have been recently developed to prepare various perovskite materials. For BFO in particular, metal nitrates (i.e. $\text{Bi}(\text{NO}_3)_3 \cdot 5\text{H}_2\text{O}$ and $\text{Fe}(\text{NO}_3)_3 \cdot 9\text{H}_2\text{O}$) have been used as universal metal sources for most BFO products, including BFO thin films [15], nanoparticles [93, 94], nanowires [95] etc. In addition to their economic advantage, metal nitrates have a low decomposition temperature which is shown to help elimination of carbon contamination in metal alkoxide [76].

2.4.1.2 Solvent

For perovskite synthesis using the sol-gel process, the organic solvents 2-methoxyethanol (2-MOE) and ethylene glycol (EG) are widely used as a substitute for a water-based solvent, due to the good solubility of various of starting reagents in these solvents [96, 97]. Both 2-MOE and EG have a linearly structured molecule, which is thought to be easier to form a dense and stable precursor molecule [97]. The growth of the linear or chainlike polymeric structure may also help the crystallization along a certain orientation, favoring the growth of oriented films

or nanostructures [97]. Moreover, the viscosity and surface tension of 2-MOE and EG are found to be highly suited to the spin-coating deposition process used for thin film fabrication [98]. One concern with using organic solvents is their toxicity, which may compromise their uptake for mass-manufacture. Compared with 2-MOE, EG has a lower toxicity; therefore, the development of EG to be used in BFO precursors and its waste treatment are important aspects to consider.

2.4.1.3 Chelating agent

Chelating agents such as acetic anhydride, acetic acid, citric acid, or tartaric acid, affect the solution viscosity and oligomeric structures during film formation [96]. Chelation reactions between the chelating agent and the metal source facilitate the gelation process under certain reaction conditions. The molecular structures of the different chelating agents determine the phases and morphologies of the final products; therefore the selection of a chelating agent is crucial in the successful fabrication of nanostructured BFO, especially when one desires BFO with specific morphologies.

2.4.2 CSD-derived BFO thin films

The crux of preparation of high quality BFO thin films by CSD is the accurate control of the Bi:Fe stoichiometry [76]. Often imprecision of the starting chemical composition and the subsequent volatilization of Bi during the annealing step leads to secondary phases or highly conductive films with very poor leakage resistance [78, 79]. To counter this problem, excess Bi is often added to the starting reagents, which brings with it its own complication through the formation of bismuth-rich phases. Hence, there remains the important need to develop an accurate understanding of the chemical reactions that result from the nature of the precursors that are employed as well as the subsequent heat treatment steps wherein the final perovskite phase is achieved.

2.4.2.1 BFO CSD precursor preparation

The precursor is often prepared by mixing metal nitrates with the organic solvent (2-MOE or ethylene glycol), followed by adding acetic anhydride as the chelation agent, as well as dehydrating the solution. These are carried out at room temperature before spin coating. The bonding chemistry of the precursor before and after the heating process has been investigated in detail by Zhang et al. [15]. After adding the acetic anhydride to the metal nitrate and 2-MOE precursor solution, acetic acid is formed as shown in Eq. 2.2. In some other reports, acetic acid is used instead of acetic anhydride [66, 99]. However, water formed as a result of the crystals from metal nitrate in this precursor system cannot be removed and may lead to precipitates during heating due to hydrolysis.



The reaction Eq. 2.2 is exothermic and the heat produced triggers the esterification reaction between 2-MOE and acetic anhydride to form acetic acid and 2-methoxyethyl acetate:



The formation of the ester 2-methoxyethyl acetate ($CH_3OCH_2CH_2OCOCH_3$) was found to be a crucial step [15]. It increases the precursor drying time during spinning and heating due to its lower vapor pressure. This serves to reduce the tendency for precipitation during gelation and consequently contributes to a more homogenous gel film. The precipitates are metal salts in the organic precursor, and they form when precursor/precursor film dries before competition of gelation due to the onset of solution saturation. The precipitates in the film can cause a bismuth and iron phase separation and lead to an inhomogeneous film with impurities. Thus, it is important to avoid precipitate formation via control over precursor recipe and following spin-coating and drying processes [15]. The vapor pressure of the precursor also increases with increased metal nitrate loading in the precursor. This means introducing excess Bi (in order to

compensate for Bi loss during annealing) via increased metal nitrate concentration is likely to promote precipitation during gelation. On the other hand a low metal nitrate concentration in the precursor may lead to an inhomogeneous and porous surface of the thin film due to a reduced amount of metal source. Therefore there is an optimal window for metal nitrate loading: a metal nitrate concentration of around 0.3M seems suitable [15].

2.4.2.2 Spin-coating process

Once the precursor with optimized stoichiometry and viscosity are ready, the next step is thin-film deposition, which is typically realized using a spin coating technique. This process includes four general steps. (1) Deposition: the precursor solution is dropped on the surface of substrate; (2) Spin-up: The substrate starts to spin and the solution flows fast outward of the substrate by the centrifugal force; (3) Spin-off: The substrate spins at a constant velocity and excess precursor is removed by the centrifugal force as droplets; (4) Evaporation: In the last part of the spinning process, the film becomes thinner due to evaporation [80]. The film thickness in the sol-gel process is largely governed by the spinning step. Film thickness after deposition strongly depends on the precursor viscosity, precursor density, spin-coating velocity and spin coating time. The relationship between film thickness and above factors can be described as [80]:

$$h(t) = \frac{h_0}{\left(1 + \frac{4\rho\omega^2 h_0^2 t}{3\eta}\right)^{\frac{1}{2}}} \quad 2.4$$

where h = film thickness at time t ; η = liquid viscosity; ρ = density of the liquid; t = time; ω = angular velocity and h_0 = initial film thickness.

Thus, thickness of films varies directly with precursor viscosity, whilst it varies inversely with solution density, spin-coating time and spin-coating velocity. However, thick films fabricated using a highly viscous precursor or slow spin-coating velocity are susceptible to defects like

cracking or phase inhomogeneity after drying. In practical situations thicker films are often obtained by repeating the spin-coating step several times to achieve the desired thickness.

The phenomenon of evaporation actually occurs during the entire spin coating process for BFO precursors. The spin coating process can even accelerate the evaporation (drying) process due to the increasing airflow rate above the films, which again promotes the formation of precipitates. It has been shown that preheating the substrates to the gelation temperature (e.g. 70° C) before adding drops of precursor onto the substrates for spin coating deposition is an effective and elegant way to avoid precipitates. The preheating possibly triggers initial gelation of the precursor layer on the heated substrate, as well as increasing the solubility of the metal nitrates in the precursor solution, thereby inhibiting precipitation [15].

2.4.2.3 Heat treatment

After spin coating deposition, heat-treatment processes are used to transform the as deposited gel-film into a crystallized BFO thin film. These heat-treatment processes include drying, pyrolysis and crystallization.

Drying

Drying is a step to remove the solvent by heating. As drying simply works on evaporation, its rate is sensitive to the temperature and vapor pressure [80]. Compared to a bulk material, thin films have a comparatively large surface area to volume ratio, so the evaporation process of a thin film is often easier and faster. As discussed above, this process can happen during spin coating and heating. For thin-film samples, gelation often happens during the drying step as well as heating. To obtain a uniform gel film after drying, it is important to ensure that the gelation step is completed before drying, so that no precipitates are formed. This can be achieved by heating the sample for gelation at a temperature higher than 70° C, followed by completely removing the remnant solvent at 270° C [15].

Pyrolysis

The drying temperature is often not sufficient to remove all the polymers in the material and a higher temperature pyrolysis process is needed before crystallization to prevent the formation of defects. Films after pyrolysis are amorphous and the nucleation and- growth process will occur in the following annealing/sintering (crystallization) process which takes place at a higher temperature [13].

Annealing

Two different high-temperature heat-treatments are often used for ceramic thin film annealing/sintering. One is the conventional heating process, by which the materials are heated slowly to a target temperature and maintained at this temperature for a specific duration (typically minutes). The other process, called rapid thermal processing, is an increasingly popular manufacturing process which heats films to a high temperature over short timescales of several seconds.

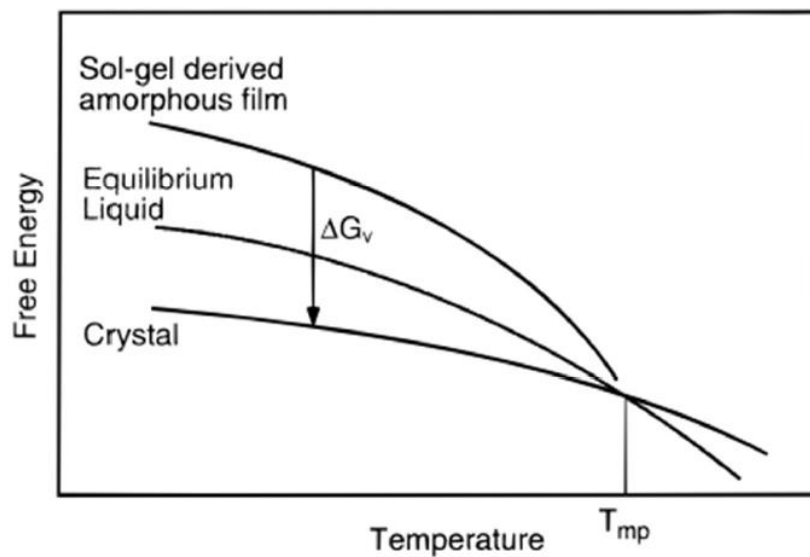


Fig. 2.16. Diagram of the free energies of a sol-gel derived amorphous film [13]

For both heat treatments, nucleation of the amorphous thin films starts first during the heating process, followed by the grain growth. The driving force of crystallization is determined by the free energy difference between the amorphous and crystallized material, and the temperature below melting point [13], as illustrated in Fig. 2.16.

During the sintering and densification process, the particles begin to join together and the pores become smaller until elimination due to the diffusion of materials driving by interfacial energy. Since the solid-vapor area to volume ratio in gel thin film is large, the driving force for sintering the gel is strong even at low temperature, making the final sintering temperature comparatively lower compared to bulk BFO processing. Nucleation often takes place either in the bulk body or the substrate-film interface of the thin-films. The former is a case of *homogeneous* nucleation, leading to random oriented grains and polycrystalline thin films. The latter case is *heterogeneous* nucleation, which often contributes to oriented columnar grain nucleation and growth matched to the substrate lattice structure. Generally, the nucleation barrier for heterogeneous nucleation is lower than that for homogeneous nucleation. The free energy diagram in Fig. 2.16 shows that a higher heating temperature decreases the driving force, thereby preventing homogenous nucleation. Therefore, rapid heating of the dried film to a high temperature promotes preferred heterogeneous nucleation at the interface thereby promoting textured or epitaxial grain growth [13, 76].

In addition to the heating rate and the absolute temperatures, even the role of ambient has been investigated in the CSD synthesis of BFO thin films. Yun et al. [100] reported that using stoichiometric BFO precursor, secondary phases, such as $\text{Bi}_2\text{Fe}_4\text{O}_9$, form when annealing at oxygen atmosphere, while polycrystalline BFO of single phase is obtained when heating at the nitrogen atmosphere. High performance polycrystalline BFO films with pure phase and high polarization have also been achieved by using a precursor with excess Bi [101] and annealing at nitrogen atmosphere.

CHAPTER 3 : EXPERIMENTAL

3.1 Precursor Solution Preparation

Precursor solution was prepared using $\text{Bi}(\text{NO}_3)_3 \cdot 5\text{H}_2\text{O}$ (Merck, India) and $\text{Fe}(\text{NO}_3)_3 \cdot 9\text{H}_2\text{O}$ (Merck, India) as Bi and Fe sources respectively and a mixture of 2-methoxyethanol (Merck, India) and acetic acid (Qualikems, India) was employed as the solvent. Although acetic anhydride was reported to be better than acetic acid in producing smoother films [15], we have used acetic acid instead because of its lower cost. Once the salts dissolve, a clear dark brown solution (Fig. 3.1) forms.

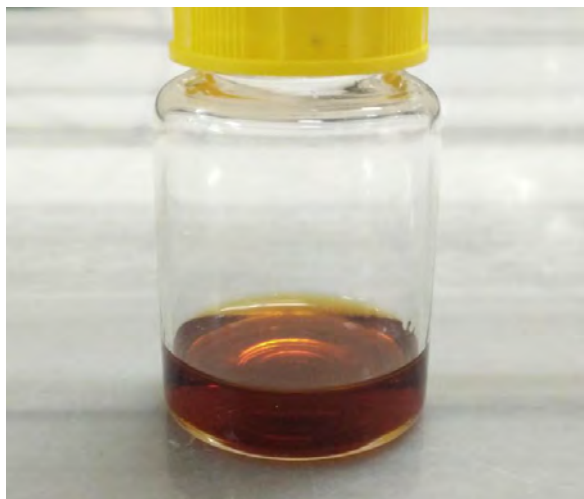


Fig. 3.1. A typical dark brown precursor solution

Two parameters of the solution were varied to see their effects on the final film. First, precursor solutions were made using a 2-methoxyethanol:acetic acid ratio of 2:1, 3:1 and 4:1 while keeping the molar ratio of Bi:Fe at 1:1. Secondly, the effect of Bi non-stoichiometry was studied by preparing solutions with Bi:Fe ratios of 0.95:1 and 1.05:1 with the ratio of 2-methoxyethanol:acetic acid fixed at 1:1. In all cases, the concentration of each metal nitrate in the solution was kept at 0.3M. In select cases, solutions were filtered using grade 42 (pore size 2.5 μm) Whatman quantitative filter papers.

3.2 Substrate Cleaning:

A proper cleaning routine is essential in producing adherent and uniform thin films. Soda-lime glass substrates were used in most experiments. For some experiments Fluorine-doped Tin Oxide (FTO) coated glass substrates were utilized. Substrates were ultrasonically cleaned in three steps:

- a) First, the substrates were ultrasonicated in a 10% NaOH solution at 55° C for 10 mins
- b) Next, ultrasonication was done in an ethanol solution for 10 mins at room temperature
- c) Finally, ultrasonication was done in de-ionized (DI) water for 10 mins at room temperature

After each of the first two steps, the substrates were rinsed in running DI water before putting them into the next bath. In some cases, combining the last two steps, i.e. cleaning once in 50/50 ethanol/DI water solution for 10 mins, did not seem to have any negative repercussions. However, following the last step, the substrates were invariably rinsed in DI water and then spun in the spin coater for some seconds to rid the substrate of the remaining water. This is done because if the wet substrates dry naturally, then water-marks remain where the last drops evaporate, causing localized de-wetting of the precursor solution when it is dispensed later on.

3.3 Film Deposition:

3.3.1 Solution dispensation

A fixed amount of solution (20-35 μ l depending on substrate size) was dispensed using a micropipette on preheated soda-lime glass substrates. Preheating temperatures of 30° C, 40° C, 50° C, 60° C and 70° C were tested. The technique of dispensing the solution was found to be very important in controlling film coverage on the substrate. Three methods were evaluated for solution dispensing:

- a) The solution was dispensed on the central region of a static substrate and then spinning was started. This is the easiest and simplest method.
- b) Dispensation was done while the substrate began rotating. This is called a dynamic dispense and can potentially give better coverage than static dispense.
- c) Static dispense but with the addition of manual spreading of the liquid with the micropipette tip to cover the entire substrate before spinning. This method requires a bit more practice as it is advisable to carry out the spreading operation without touching the tip to the substrate surface. Since our substrates had to be preheated as well, this meant that the procedure had to be done quickly in order to avoid a substantial loss of substrate temperature.

3.3.2 Spinning and heating schedule

A spin coater (MIDAS Spin-1200T) was used to deposit the films using the following recipe based on ref. 15: in 15 seconds the substrate was accelerated to 3000 rpm, spun at that speed for 40 s and then spun at 6000 rpm for 10s. During the 3000 rpm spinning the film becomes moderately rigid and hence the 6000 rpm spin only serves to quickly evaporate any remaining solvent.

After spin coating, the films were heated at 90° C for 1 min for gelation and dried at 270° C for 3 min for drying. Substrate preheating, gelation and drying were done on top of a hot plate. The entire procedure was repeated as many times as required (generally three times) to obtain the desired thickness of the films. At this point an amorphous organo-metallic film is present. To remove the organic components the films were first pyrolyzed at 450° C for 30 mins and then annealed/sintered for another 30 mins for crystallization and phase formation to take place, in a muffle furnace. Annealing temperatures of 450° C, 500° C, 550° C and 600° C were tested. Heating rate was 3° C/min and samples were cooled slowly in the furnace. Fig. 3.2 shows a

typical 3 layer film produced by this method (annealed at 550° C). Apart from areas near the edges and corners, a moderately uniform film was obtained.



Fig. 3.2. A typical 3 layer film after annealing

A select few experiments were done in which rapid heating was accomplished by inserting samples into a furnace already heated to 450° C. Subsequent heating schedule was kept the same as that for slowly heated samples.

A seed layer was also synthesized by making a 1 layer thin film, i.e., a film where only one spin coating cycle was done. This was then put through the usual heat treating schedule to get a thin BFO layer. Afterwards, two more layers were deposited on top of the annealed 1 layer film, and a final annealing was done to crystallize the final two layers.

3.4 Film Characterization:

3.4.1 Topography and microstructure

Initial morphology and topography of the films were observed using an optical microscope. This gave an idea about the surface smoothness and continuity of the films at different stages of the heat treatment process. Surface of the annealed films were observed using a field emission scanning electron microscope (FESEM: JEOL JSM 7600F) to ascertain the grain

size/distribution/shape as well as absence/presence of voids or micropores. Cross-sectional SEM images were also obtained to get an idea about film thickness. Since BFO as well as glass is insulating, the surface that is to be observed was gold coated in a sputter coater. The substrates had to be cut into smaller pieces in order for them to fit into the SEM sample holder.

3.4.2 Phase analysis

Diffraction patterns of as deposited annealed films were obtained in the usual Bragg-Brentano geometry (not Grazing Incidence/GIXRD) using an X-ray diffractometer (Empyrean, PANalytical) for phase and structural analysis. The diffractometer was equipped with a Cu-target producing Cu K α_1 ($\lambda = 1.540598 \text{ \AA}$) and Cu K α_2 ($\lambda = 1.544426 \text{ \AA}$) radiation with intensity ratio of (K α_1 /K α_2) 0.5. GIXRD was not employed because we had wanted to obtain information about any possible texture present in the films which would be difficult in GIXRD.

3.4.3 Electrical characterization

For electrical characterization, several methods were attempted:

- a) Usually the best and most used method to measure electrical properties of insulating thin films is to create a metal-insulator-metal (MIM) structure. With that in mind, films were deposited on Fluorine doped Tin-Oxide (FTO, a transparent conducting oxide) coated glass substrates (Techinstro, India) according to the method outlined in the preceding sections. After annealing, circular gold electrodes with diameters such as 3 mm, 2 mm, 1.4 mm, 1.2 mm, 1 mm and 0.8 mm were sputtered on top of the films using a shadow mask and deposition time of 150 – 180 seconds (Fig. 3.3(a)). Next, a small area of the BFO film was etched using HCl solution so that the FTO layer underneath could be accessed – HCl solution was found to be effective at dissolving BFO without causing detectable damage to FTO. Hence an MIM structure was formed with FTO acting as the bottom electrode and gold acting as the top electrode. In this case, the

length of the current path would be equal to the thickness of the films and the cross-sectional area of the current path would equal the area of the top electrode. The large

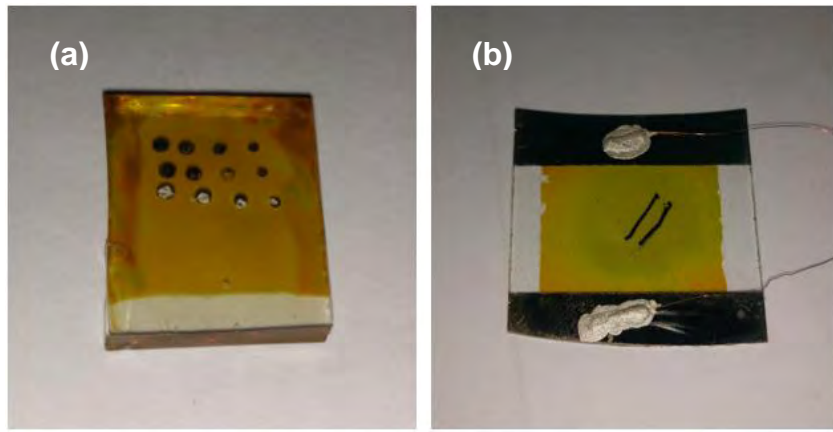


Fig. 3.3. (a) Gold electrodes sputtered on top for MIM structure and (b) planar configuration of electrodes. Two wires were attached using silver paste

area of the bottom electrode is ignored in this geometry because the films are so thin; the currents do not get a chance to diverge appreciably from the area defined by the top electrode. The advantage of this method is that it gives the most reliable and accurate measure of the film's electrical characteristics provided the film is of sufficiently high quality. Another advantage is the tiny length of the current path, usually around a few hundred nanometers, which gives a low resistance between the probes even in highly insulating films. Getting a high quality film is not always easy however, and that is this method's biggest disadvantage. This method is especially sensitive to through thickness defects, cracks, pinholes, extraneous particles, porosity etc. Since a single critical flaw that falls under the area defined by a top electrode can ruin the reliability and/or accuracy of measurements using that electrode, it is vital to make the top electrodes as small as practically possible so that the probability of a defect free area of the film being sampled under the electrode is increased.

- b) In another method, a planar configuration of electrodes were used. Films deposited on uncoated glass substrates were used and a rectangular region of the films were defined

by etching away the sides of the film. Two rectangular gold electrodes were sputtered on two opposing edges of the film as shown in Fig. 3.3(b). Here, the two electrodes would act as two terminals and the current would flow parallel to the substrate along the film. In this case, the length of the current path can be taken as the separation between the two electrodes and the area of current path is equal to the thickness of the film times the length of the film side perpendicular to the electrodes.

- c) Four point probe method was also employed to measure the resistivity. This method requires placing four equally spaced metallic probes on the surface of the films. The four points of contact form a straight line (Fig. 3.4). A current I is passed through the two outer probes while the voltage drop V between the two inner probes is detected, from which the resistivity of the film can be calculated using the following formula [102].

$$\rho = t \frac{\pi}{\ln(2)} \frac{V}{I} \quad (3.1)$$

Here t is the thickness of the film. The equation is only valid for sufficiently thin films and films with side lengths much greater than the probe separation S . One advantage of the four point probe method is that it requires no electrodes to be manufactured as the probes are made to touch the film surface directly.

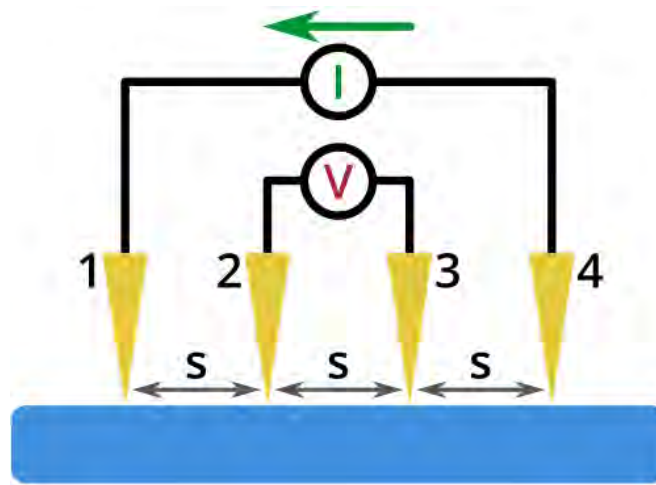


Fig. 3.4. Four point probe setup

3.4.4 Magnetic and optical characterization

A Vibrating Sample Magnetometer (VSM: Microsense) was used to measure the magnetization of the thin films. Substrates with films had to be cut into small sizes (maximum dimension <10 mm) for them to fit in the gap between the Helmholtz coils that generate the magnetic field.

In order to determine the band gap and absorption properties of the thin films, UV-Vis spectroscopy (Perkin Elmer, Lambda 1050) was carried out.

CHAPTER 4 : RESULTS AND DISCUSSIONS

4.1 Role of Dispensing Method:

To ensure coverage of the entire substrate with the precursor solution before the excess liquid is spun off, a very good wetting between the solution and substrate is required. However, such levels of wetting was not achieved for the current combination of soda-lime glass and precursor solution. This was revealed by the incomplete coverage of the substrate under normal static dispensation of the solution. The appearance of the film made using this method is shown in Fig. 4.1. As can be seen the substrate is only partially covered. The excess liquid seems to have flung off from the substrate before coating the entirety of the surface. Dynamic dispense sometimes gave complete coverage but at other times it produced films like that shown in Fig. 4.1.

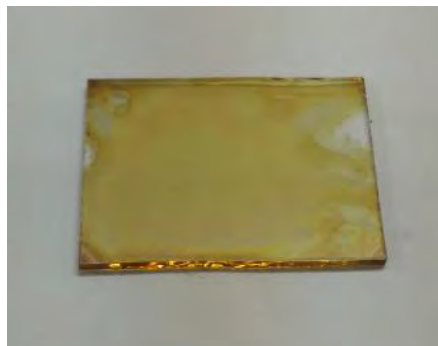


Fig. 4.1. Incomplete coverage of the substrate in static dispense

The third method, which involved dragging/spreading the liquid with the micropipette tip before spinning, was found to consistently produce full coverage of the substrate (see Fig. 3.2). It should be mentioned that when spreading the solution, if enough liquid is not dispensed then fully covering the substrate with a liquid film *before* spinning is not possible. During manual spreading, the solution tends to shrink back and form a pool in the center. However, this was found to not be an issue - the solution leaves a thin residue in areas where it was once spread

but might have subsequently shrunk away from. This residue improves the wetting characteristics greatly, making the solution cover the substrate uniformly once spinning begins.

4.2 Film Topography and Structure:

4.2.1 Effect of preheating

Preheating of the substrate was found to play a very important role in controlling the topography of the films. We did not, however, face issues with precipitation of metal salts. Low substrate preheat temperature caused discontinuous (on the micro scale) films to be produced while higher preheat temperatures seemed to mitigate the issue. Details are given in the following paragraphs.



Fig. 4.2. Film appearance after drying using different preheat temperatures (a) 30° C, (b) 40° C, (c) 50° C, (d) 60° C and (e) 70° C

When the substrate was preheated to 30° C (basically equivalent to no preheating) the films did not show any apparent problem right after spinning. However, as soon as the substrate was heated to 90° C for gelation, the film rapidly took on a whitish appearance. After the drying step, the film developed a slight yellowish brown hue, characteristic of BFO, but the whitish areas still dominated the visual as seen in Fig 4.2. Interestingly, there was a blue tinge in the whitish areas and these areas were much more perceptible when light struck the film obliquely rather than straight on. At 40° C, Fig. 4.2(b), the whitish areas can still be seen to be largely present but the central area of the film looked clearer. Subsequent increase of the preheat temperature to 50° C and 60° C served to shrink the white area towards the outer regions and

an increasingly large area around the center was taking on a clear yellowish color. At 70° C, the film was totally clear. This transition is shown sequentially in Fig. 4.2.

The blueish tinge given off by the milky regions suggested a scattering process, because blue light is scattered most strongly. Optical micrographs presented evidence that this is indeed the case. Fig. 4.3 shows the optical micrograph of the film preheated at 30° C, and it is obvious that the film was not smooth. In fact, a look at higher magnification reveals that the “film”

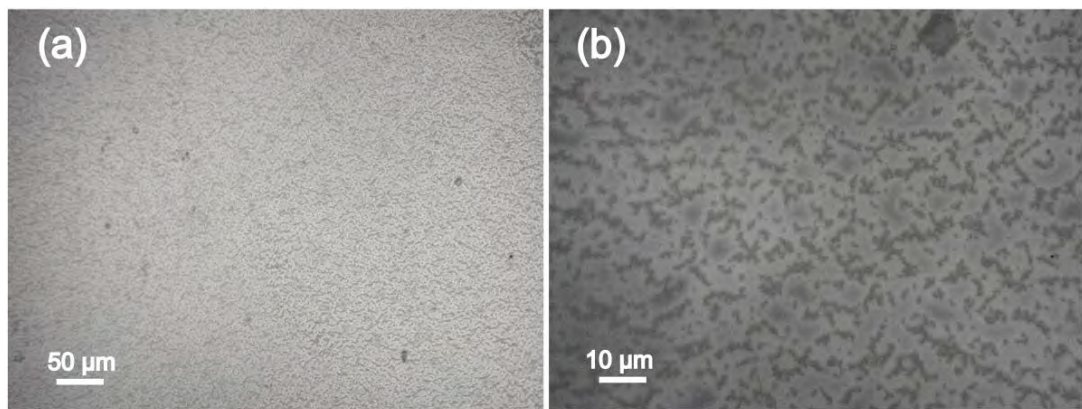


Fig. 4.3. Optical micrograph of dried film deposited using 30° C preheat at magnification (a) 200x and (b) 1000x

actually consists of separated islands of dried solution. Dark regions are the actual “film” as demonstrated by the features indicating roughness that is apparent when looked at carefully. The white areas are simply the glass surface as recognized by its featureless and smooth façade. It is these microscopically separated dark regions which cause light scattering and give off a blueish hue.

The continuity of the films increased with increasing preheat temperature. Fig.4.4 shows the micrographs of the white areas of films that were deposited on substrates preheated to higher temperatures than 30° C. It is readily observed that the discontinuity in the films significantly drops with increasing preheat temperature and for 70° C preheat, the micrograph (Fig. 4.4(d)) is nearly featureless indicating a smooth surface. As already mentioned we have observed that,

at intermediate preheating temperatures the central region became gradually clearer while the whitish region was relegated to the outward regions. Under the microscope, the clearer regions

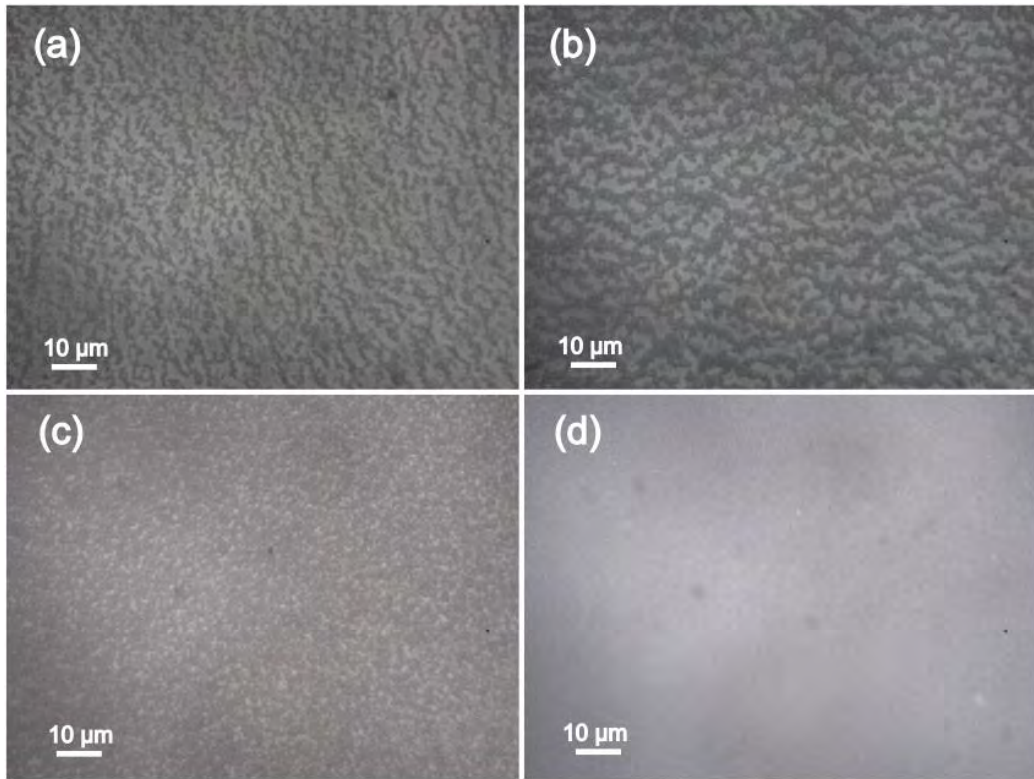


Fig. 4.4. Optical micrographs of dried films deposited using preheat temperatures of (a) 40° C, (b) 50° C, (c) 60° C and (d) 70° C at 1000x magnification

present a much smoother topography while the peripheral regions consist of uneven and discontinuous films as before. Representative pictures are shown in Fig. 4.5. Hence, in this case at least, we have observed a direct correspondence between the macroscopic appearance of the film with the microscopic topography and film smoothness/contiguity.

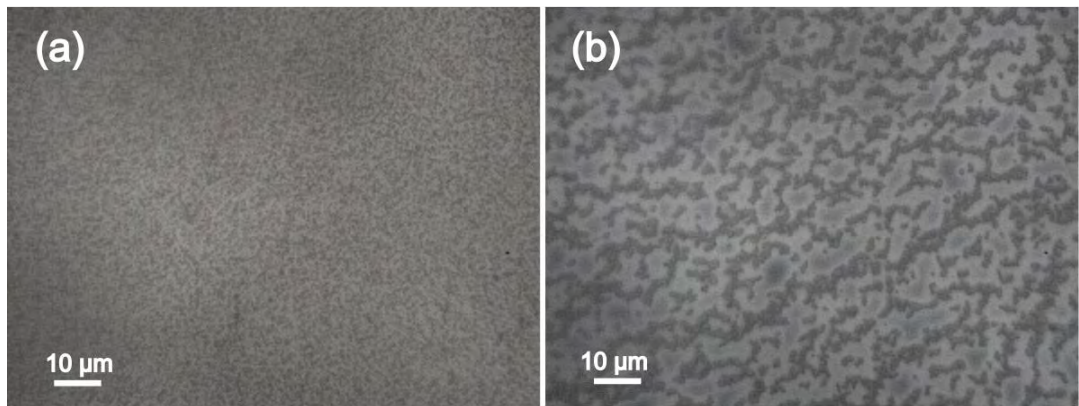


Fig. 4.5. Optical micrographs of dried film deposited using 50° C preheat showing (a) the central clear area and (b) the whitish peripheral area at 1000x magnification

After annealing at 550° C, all films underwent crystallization. The island like dark regions became clearer and showed obvious clusters under the microscope. Although under the optical

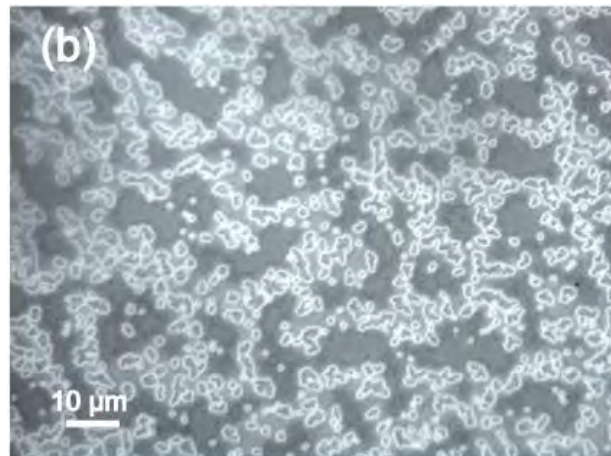


Fig. 4.6. Optical micrograph of annealed film deposited using 30° C preheat at 1000x magnification

microscope it seemed as though these islands contained large single grains (Fig. 4.6), in reality these contain innumerable tiny grains as shown in Fig. 4.7(a), for 30° C preheating. For higher temperature preheating, the microstructure gets better, ultimately consisting of more or less equiaxed grains of size less than 100 nm for 70° C preheat as depicted in Fig. 4.7(b).

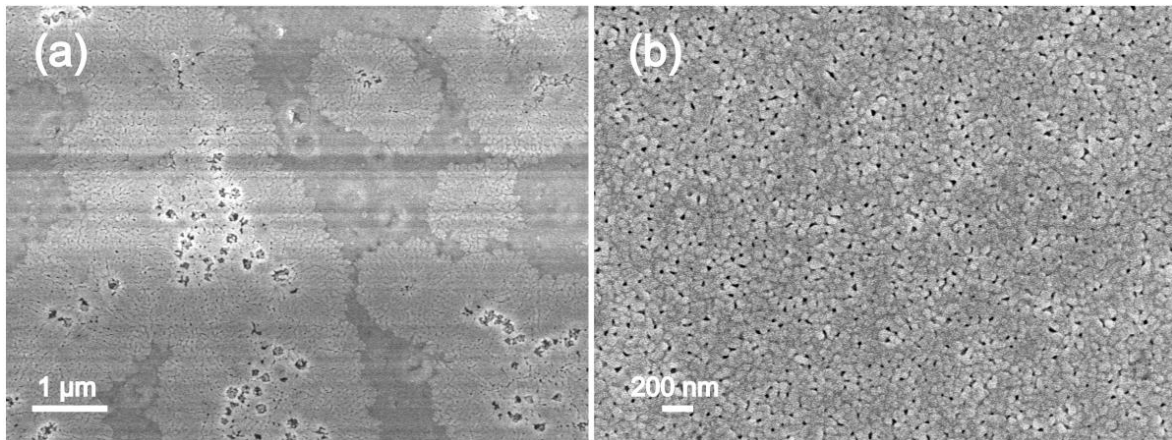


Fig. 4.7. SEM images of annealed films deposited using (a) 30° C and (b) 70° C preheat

Diffraction patterns of films made under different preheat conditions are shown in Fig. 4.8. Despite the very low signal coming from these 1 layer thin films, the occurrence of BFO with its rhombohedral perovskite structure can be inferred with reasonable certainty. That this is the case will be made apparent later for thicker films. For now, we note that the peaks got more pronounced at higher preheating temperatures. It seems that, because of the films' increased continuity, the diffracting volume gets larger at higher preheat temperatures making the peaks more intense. Note that the hump like background observed up to $2\theta \sim 40^\circ$ is the contribution of the amorphous glass substrate. Hence, the preheat temperature is significant so long as topography of the film is concerned; it has no bearing on the phase formation from or crystallization of the as dried amorphous films.

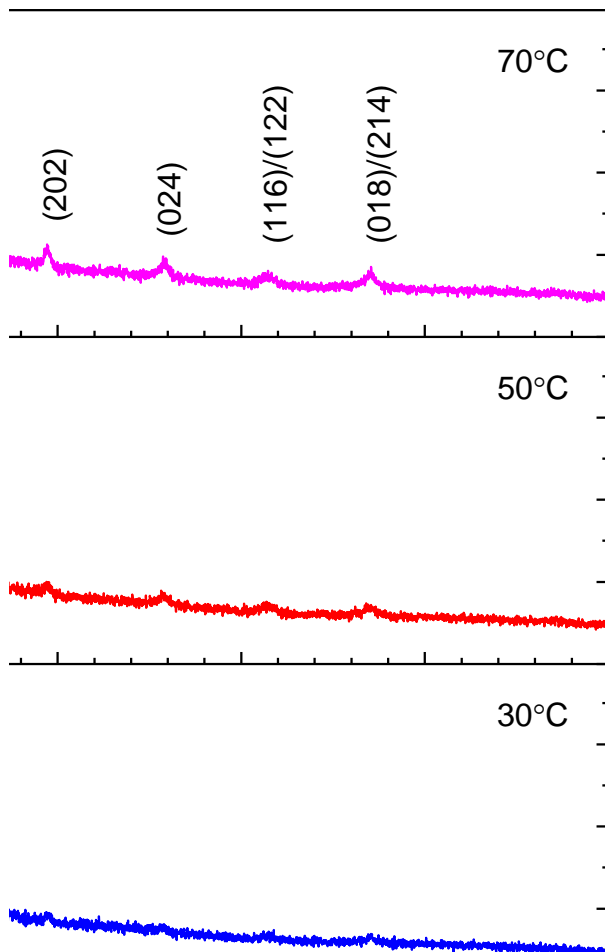


Fig. 4.8. XRD pattern of annealed films deposited using preheat temperatures of 30° C, 50° C and 70° C; peaks labeled according to hexagonal unit cell

The mechanism behind the films being discontinuous at low preheat temperatures is not exactly clear. Perhaps at higher temperatures the solvent gets evaporated to a higher extent and when gelation occurs, the films do not shrink as much. Shrinkage does seem to be the physical cause behind film discontinuity. There are two observations that support shrinkage as the cause-

- a) The sides of the films were more discontinuous than the center. A uniformly shrinking body shrinks toward the center of mass and parts of the body that are further from the center experience larger displacements compared to parts that are closer to the center.

- b) The discontinuous regions of the films were not comprised of separated equiaxed islands but rather elongated ones, clearly seen for example in Fig. 4.4(a). The general direction of elongation in an area differed depending on its location on the substrate. In fact, the elongation direction was observed to be tangential with respect to the center of the film.

Such observations are consistent with the scenario that during gelation, the film shrinks toward the center of the substrate, radially pulling the outward regions of the film inwards. This pulling force overcomes the adhesion between the wet film and the substrate, causing the film to lose continuity. Farther away we go from the center the greater is the pulling force and hence higher is the degree of discontinuity. Since the force is radial in nature, the “tears” that occur in the wet film is perpendicular to the direction of the force which is why we have seen the elongated regions to be arranged tangentially with respect to the center.

One might imagine that, this added degree of control over film topography at the microscopic level could be put to use where controlled roughness/discontinuity might be desirable such as in photocatalytic applications.

4.2.2 Role of solvent ratio

The ratio of 2-methoxyethanol to acetic acid was varied as 2:1, 3:1 and 4:1. The appearance or film morphology under the optical microscope did not seem to depend on the solvent ratio (images not shown). Even at various preheat temperatures, the general trend of increasingly continuous films with higher preheat temperatures persisted for any solvent ratio. Annealed films showed no significant dissimilarity in phase formation between films synthesized from solutions with different solvent ratio, as apparent from the XRD patterns (Fig. 4.9). The SEM images, as shown in Fig. 4.10, does seem to capture some change. Voids present in the annealed films can be seen to go down as solvent ratio is increased from 2:1 to 4:1.

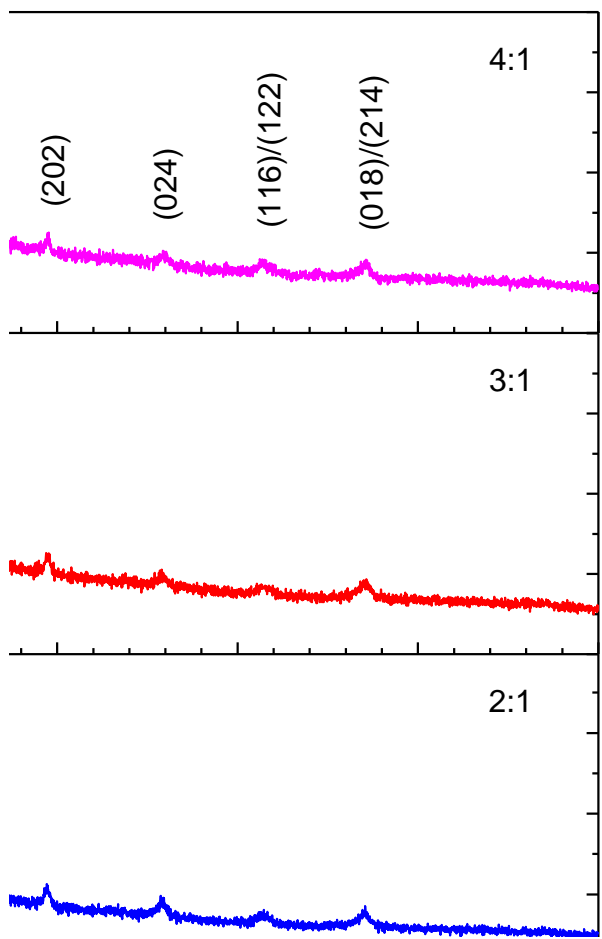


Fig. 4.9. XRD patterns of films deposited using precursor solutions with 2-MOE:acetic acid ratio of 2:1, 3:1 and 4:1; peaks labeled according to hexagonal unit cell

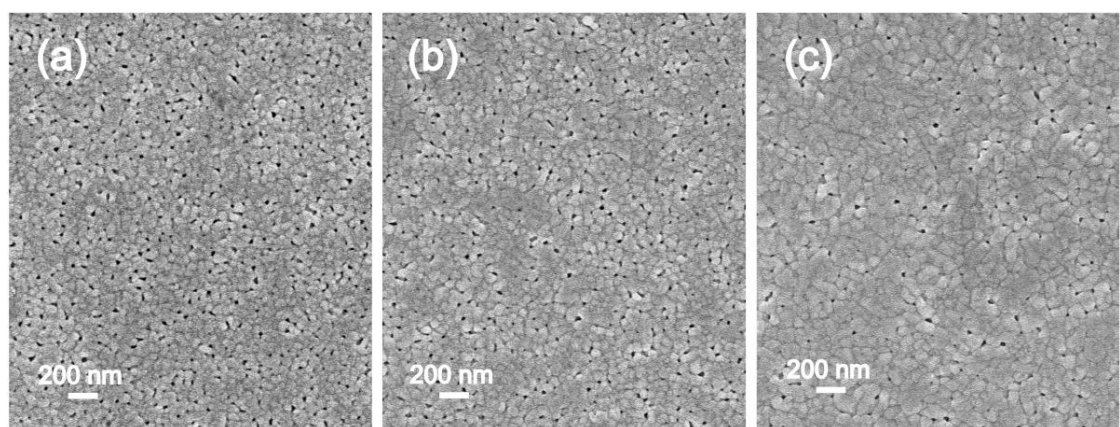


Fig. 4.10. SEM images of films deposited using precursor solutions with solvent ratio of (a) 2:1, (b) 3:1 and (c) 4:1

Theoretically one would expect there to be a lower limit to the amount of acetic acid that has to be used because it plays an essential role in the gelation process of the films as discussed in the literature review section. In our experiments this limit was apparently not reached. However, the reduction of voids in the films with increasing solvent ratio suggests that excess acetic acid in the solution is detrimental to dense microstructure formation. It's possible that after the drying stage, acetic acid has a greater tendency to remain in the film, in whatever form, as an organic residue compared to 2-methoxyethanol. If such is the case, during pyrolysis, more organics will have to be burned off in the film made using a higher acetic acid content (i.e. lower solvent ratio) than the film made using a lower acetic acid content (higher solvent ratio). Thus, the decrease in voids as solvent ratio goes up might be ascribed to a decrease in the amount of organics that are removed during the pyrolysis stage.

4.2.3 Effect of annealing temperature

After the drying step the film that is present is in an amorphous state. Annealing at high temperatures is required to form BFO. The films were annealed at four different temperatures to find the most suitable one for desired phase formation and suppression of secondary/parasitic phases. Unless otherwise noted, all films discussed from this point on, were made from a precursor solution of 2:1 solvent ratio and on a 70° C preheated substrate. XRD patterns of the films annealed at 450° C, 500° C and 550° C are shown in Fig. 4.11(a).

Fig. 4.11. (a) XRD patterns of films annealed at 450° C, 500° C and 550° C; “*” denotes peaks not belonging to BFO. (b) Magnified portion of the patterns from 2θ=22°- 23° showing shifting of the (012)_h/(100)_{pc} peak; peaks labeled according to hexagonal unit cell

It can be clearly seen that the rhombohedral phase of BFO is the dominant one when the film was annealed at 550° C, and also when annealing temperature was 500° C although to a lesser extent. 450° C was deemed to be inadequate for full formation of the rhombohedral BFO phase as apparent from the multitude of observable peaks in the diffractogram that do not belong to BFO. The unit cell of BFO was also observed to expand with increasing annealing temperature as evidenced by the shifting of peaks to the left. Fig. 4.11(b) depicts this shift for the (012)_{hexagonal(h)} or (100)_{pseudo-cubic(pc)} peak. Annealing temperature of 600° C was also tested but that film’s XRD pattern did not have any peaks – only the amorphous hump was present. At

such a high temperature the film probably gets incorporated into the glass itself which is simply a result of the low softening point of the ordinary glass that was used.

Fig. 4.12 shows the SEM images of the films annealed at different temperatures. The well-developed grains seen in the film annealed at 550° C (Fig. 4.12(c)) supplements its diffraction

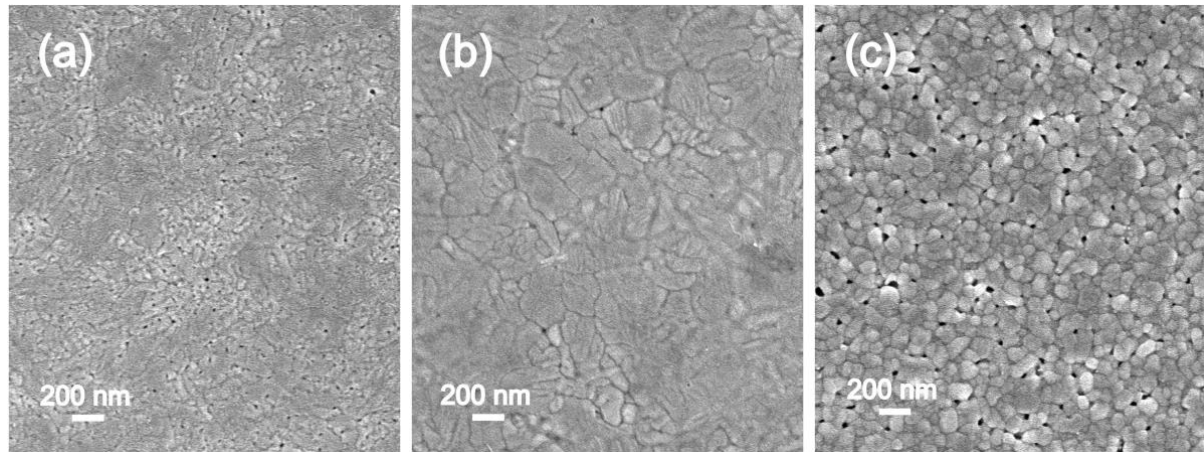


Fig. 4.12. SEM images of films annealed at (a) 450° C, (b) 500° C and (c) 550° C

pattern in the sense that the homogeneity of the microstructure implicates phase purity. For the other two cases a similar association was apparent – the film annealed at 450° C presented a microstructure where well developed grains were not abundant while the microstructure at 500° C did have grains but not as equiaxed and uniform as that of the film annealed at 550° C. The microstructural images thus correlates agreeably with the diffraction patterns. At the lower annealing temperatures, microstructural changes may not have occurred that much and the film resembles the as dried condition. On the other hand, during annealing at 550° C recrystallization is obvious giving rise to the observed homogeneous grain structure. Therefore, even though the film annealed at 550° C has some porosity (Fig. 4.12(c)) when taking into account the overall microstructure and phase purity, this temperature can be deemed to be the best among those presented here.

4.2.4 Effect of heating rate

Some films were rapidly heated to the pyrolysis temperature and then annealed in the usual way to ascertain the role of heating rate. The central region of the rapidly heated films had a very slight white appearance once more, indicating some irregularity in the film microstructure. Indeed, optical micrographs (Fig. 4.13) revealed patterns of slightly dark marks throughout the central region of the film but such marks were absent towards the sides where there was no white visible to the naked eye. These might be artefacts resulting from rapid gas evolution during pyrolysis.

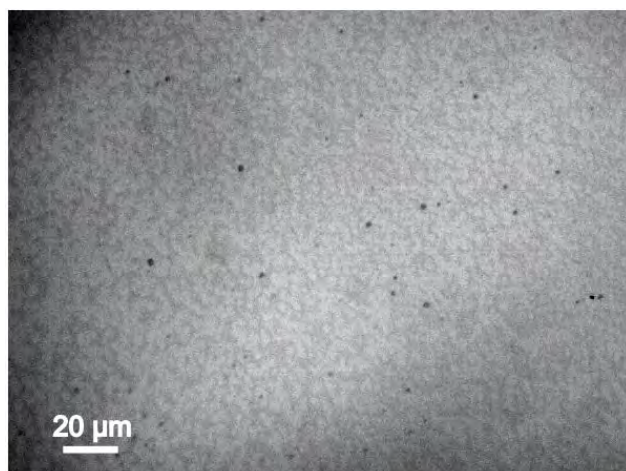


Fig. 4.13. Optical micrograph of central region of rapidly heated film at 500x magnification

On the other hand, rapid heating resulted in rather unsatisfactory phase formation, as revealed by its XRD pattern depicted in Fig. 4.14. Some parasitic secondary phases are present but the peaks are not the same ones that appeared when samples were annealed at 450° C (Fig. 4.11). Perhaps at different stages of the pyrolysis/annealing cycle different phases appear and disappear again. When the films were annealed at 450° C, the temperature was insufficient to cause full reaction and form BFO. During rapid heating, perhaps more than one phase preferentially nucleates at the glass surface induced by local variations in concentration. These secondary phases might then persist afterwards.

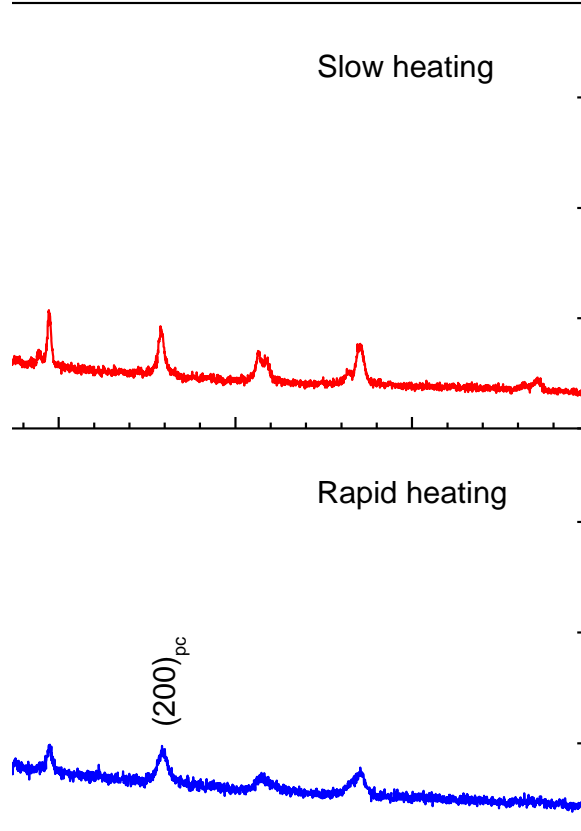


Fig. 4.14. Effect of heating rate on the XRD pattern; Bi:Fe ratio and annealing temperature were kept same

The more interesting aspect seen from the XRD pattern however, is the emergence of a preferred orientation. The first peak is more intense than usual indicating a possible $(100)_{pc}$ texture which is further proved by the prominence of the $(200)_{pc}$ peak also. We think this arises because rapid heating encourages heterogeneous nucleation on the glass surface and the grains thus formed grow along the $(100)_{pc}$ direction most quickly. Further discussion of this aspect is deferred until section 2.2.6.

4.2.5 Effect of Bi non-stoichiometry

To study the effect of bismuth non-stoichiometry, films were produced with Bi-deficiency ($\text{Bi}_{0.95}\text{FeO}_3$: S1) and Bi-abundance ($\text{Bi}_{1.05}\text{FeO}_3$: S3). We will denote the film with

stoichiometric Bi concentration S2. XRD patterns of the films are shown in Fig. 4.15. All three films were well crystallized and parasitic/secondary phases were not prominent in any of the films which hint at the good stability of the rhombohedral perovskite phase with respect to small off-stoichiometry in Bi. Some peak shifting was again observed which translates to expansion or contraction of the unit cell. The unit cell expanded in going from S1 to S2 and then slightly contracted in S3 (Fig. 4.15(b)). A slight preferred orientation along $(100)_{pc}$ can also be observed in S1, the reason for which is unknown.

Fig. 4.15. (a) XRD patterns of S1, S2 and S3 annealed at 550° C; (b) Magnified portion of the patterns from $2\theta=22^\circ$ - 23° showing shifting of the $(012)_h/(100)_{pc}$ peak

Since S1 is Bi-deficient, Bi-vacancies (V_{Bi}) are expected to form which could be the cause of lattice contraction compared to S2. Fe-interstitials, which would expand the lattice, could also form but are less likely. Similarly, the Bi-rich S3 sample would likely have Fe-vacancies (V_{Fe})

or Bi-interstitials, the former being more probable, which would again cause lattice contraction. The reason for S3's unit cell being larger than S1's could be two fold – a) Bi³⁺ ion being larger than Fe³⁺ [38], its absence could cause a greater contraction of the unit cell which would mean the composition where Bi-vacancies are dominant (S1) would have a smaller unit cell compared to where Fe-vacancies dominate (S3) and (b) S2 is in reality a Bi-deficient film because of Bi-volatility during annealing [103]. To elaborate on the 2nd point, if S2 is actually Bi-deficient then upon gradual increase of Bi in the precursor, the lattice would expand until stoichiometry is reached; beyond that, however, the lattice would start to contract again eventually contracting further than the initial lattice of S2 and this might be the region where S3's composition lies.

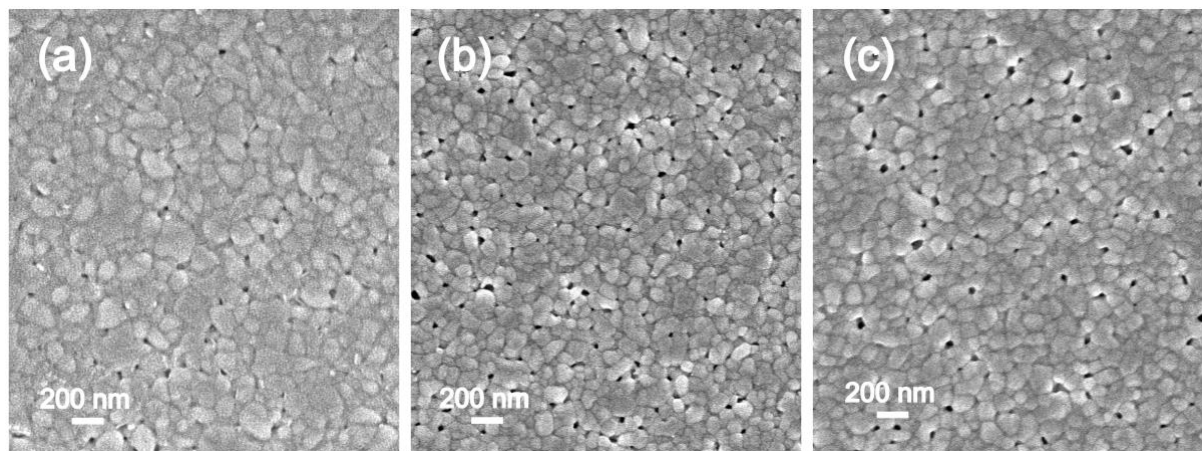


Fig. 4.16. SEM images of (a) S1, (b) S2 and (c) S3 annealed at 550° C

The microstructure of these films are shown in Fig. 4.16. It can be seen that all three films are well crystallized and the grains in each film are of a similar size. Porosity was apparent in all three films, but less so in S1. Average grain size of S1 is visibly larger than the other two, perhaps because of the presence of more vacancies in this film. Any vacancy represents empty space in the lattice and hence increases the diffusion rate of atoms [104]. Thus, from a microstructural point of view, Bi-deficiency could be beneficial.

4.2.6 Effect of seed layer

Up to this point, it has been obvious that the grains in the annealed films are generally quite small and almost completely randomly oriented. BFO is a candidate for use as a ferroelectric component in devices and to utilize the ferroelectricity of the material the grains should be large and textured in a favorable manner. Towards that end, films were made with a seed layer to see if heterogeneous nucleation at the seed layer surface can increase the grain size and/or induce texture in the films. Fig. 4.17 shows the cross-sectional image of the seed layer. It shows that it's about 100 nm in thickness or 1/3rd our usual 3 layer films. Its XRD pattern was the same as Fig. 4.9. Unfortunately, the desired improvement in microstructure or grain orientation was not observed in the final film deposited with the seed layer on the bottom. Fig. 4.18 depicts the XRD pattern of the seeded film (bottom figure) which does not show any sign of texture or preferred orientation.

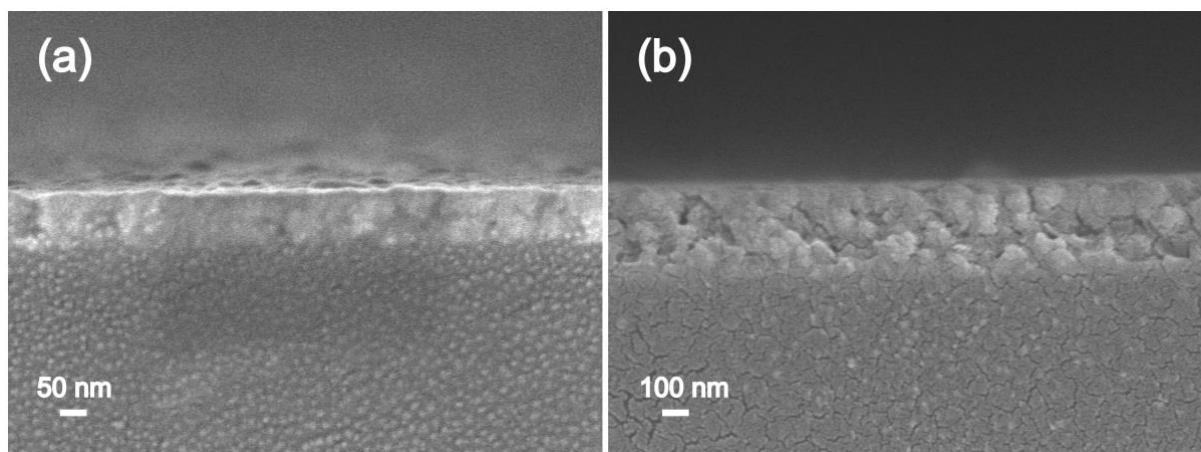


Fig. 4.17. Cross-sectional SEM images of (a) seed layer and (b) usual 3 layer film

The expected outcome was that since nucleation is required to form crystals from the amorphous film which is present before annealing, the surface of the seed layer would serve as heterogeneous nucleation sites. Generally the equiaxed type of small grains that we have

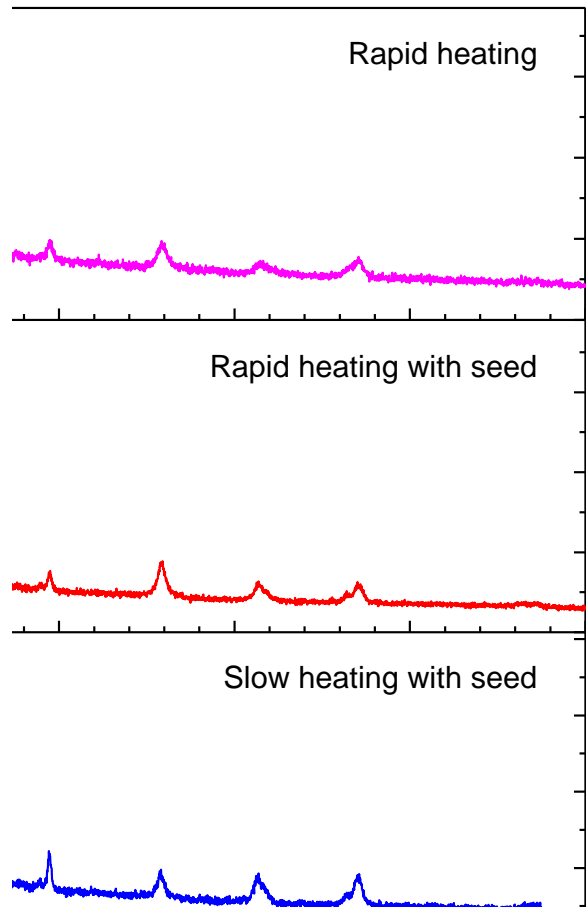


Fig. 4.18. XRD patterns of seeded and normal films heated at different rates

observed in our normal films, suggest homogeneous nucleation had occurred throughout the bulk of the amorphous film. But in the seed layer, billions of BFO grains are already present which could help reduce the surface free energy of nucleating crystals by allowing the new crystals to form on top of the old ones. In such a case, these heterogeneous nucleation events would occur before or predominantly over homogeneous nucleation in the bulk, causing all subsequent grains to grow from the bottom up. It is not likely that all crystal faces of BFO would grow at the same rate; therefore the grains that have their orientation such that their fastest growing plane faces the top surface will outgrow the other ones. Such a scenario would show up as a development of preferred orientation in XRD patterns.

The fact that the XRD pattern suggests random crystal orientation means that such a scenario does not play out. Most likely, the seed layer fails to act as heterogeneous nucleation site for the crystallizing film. A reason for this could be the fact that, the lower the temperature the higher is the driving force for nucleation – be that homogeneous or heterogeneous [13]. Since our films had to be pyrolyzed at 450° C, during which substantial crystallization begins (Fig. 4.11(a)), it is possible that at that low a temperature or even before 450° C is reached, the driving force is so large that heterogeneous nucleation is not appreciably favourable from an energy and kinetics point of view. Such behaviour has been observed before for oxide films [105].

In order to try to induce heterogeneous nucleation in the films, rapid heating of a seeded film as in section 4.2.4 was performed. Conforming to our expectations, this time a prominent preferred orientation along the (100) plane was detected from the XRD pattern, Fig. 4.18. For comparison, the XRD pattern of a rapidly heated un-seeded film is also shown. Clearly, the seeded film which was rapidly heated shows a higher degree of preferred orientation than the un-seeded film. But more importantly, the secondary phases that emerged in the case of rapidly heated un-seeded film are no longer present in the seeded film. The reason seems to be that, since there are already BFO crystals present in the seed layer, heterogeneous nucleation of only the BFO phase occurs; other phases that emerged in the un-seeded case were suppressed since they would have to overcome a higher energy barrier to nucleate on existing crystals of a different structure (i.e. BFO). Attaining preferred orientation/texture in spin coated oxide films on glass substrates is rather uncommon. Hence we believe our results here do have some novelty and merits further investigation in the future.

4.2.7 Effect of substrate

As mentioned earlier, some films were made on FTO-coated glass substrates to facilitate electrical characterization of the films. During deposition and spinning, the wettability of FTO

was found to be somewhat better than bare glass. However, this had little or no influence on the final film quality as SEM image and XRD pattern both resembled films deposited on bare glass substrates, as shown in Fig. 4.19. Of course, the XRD pattern contained peaks belonging to FTO, which in this case are easily identifiable since they occur at widely different angles (except one peak at $\sim 2\theta = 52^\circ$) compared to BFO.

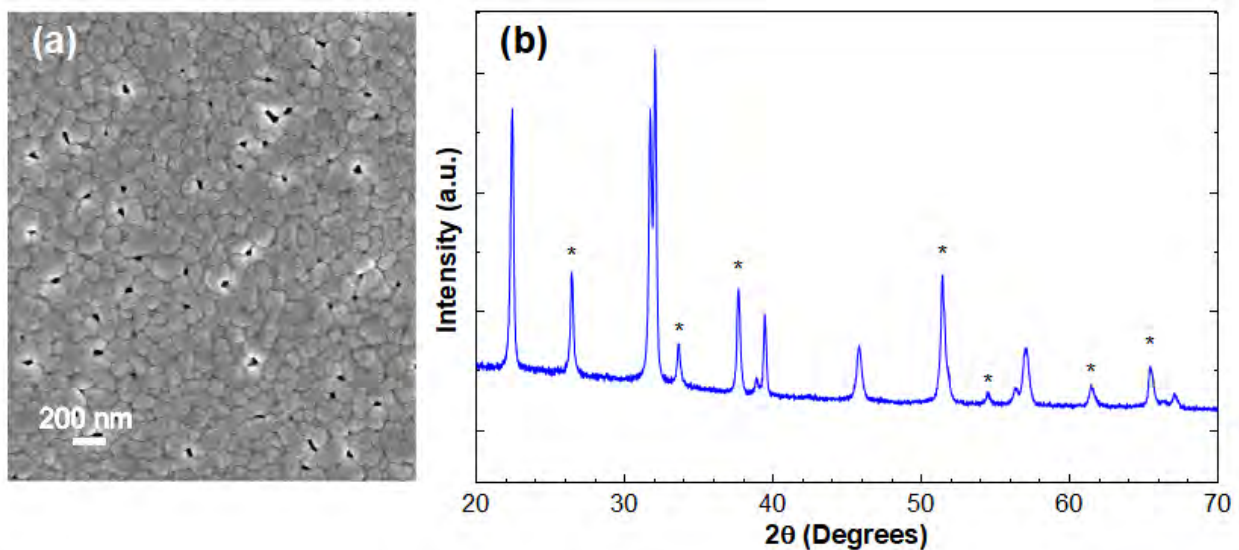


Fig. 4.19. (a) SEM image and (b) XRD pattern of BFO deposited on FTO coated glass substrate; '*' denotes peaks belonging to FTO

4.3 Electrical Characterization:

Electrical characterization of the films could not be done in most cases due to various problems. The different configurations presented different problems but ultimately a reliable measurement of the electrical characteristics of the films were not obtained. Here we discuss each configuration and state the problems that were faced in each case.

4.3.1 MIM configuration

Ideally, this method should have given the most reliable the results. However, spin coating being a chemical solution deposition process, it was impossible to synthesize films of

sufficiently high quality to allow electrical measurements to be carried out reliably. The major difficulties were as follows:

- a) In the first few attempts the top electrodes were found to be shorted to the bottom electrode (FTO layer). Since sputtering is an atom by atom process, the gold can get into crevices or cracks that are very small in size and reach the bottom of the film. In order to overcome this, thicker films of 6 layers were manufactured. The outcome was better in that some non-shorted electrodes were found. All electrodes deposited on top of the film were not usable however; some or even many electrodes were still shorted.

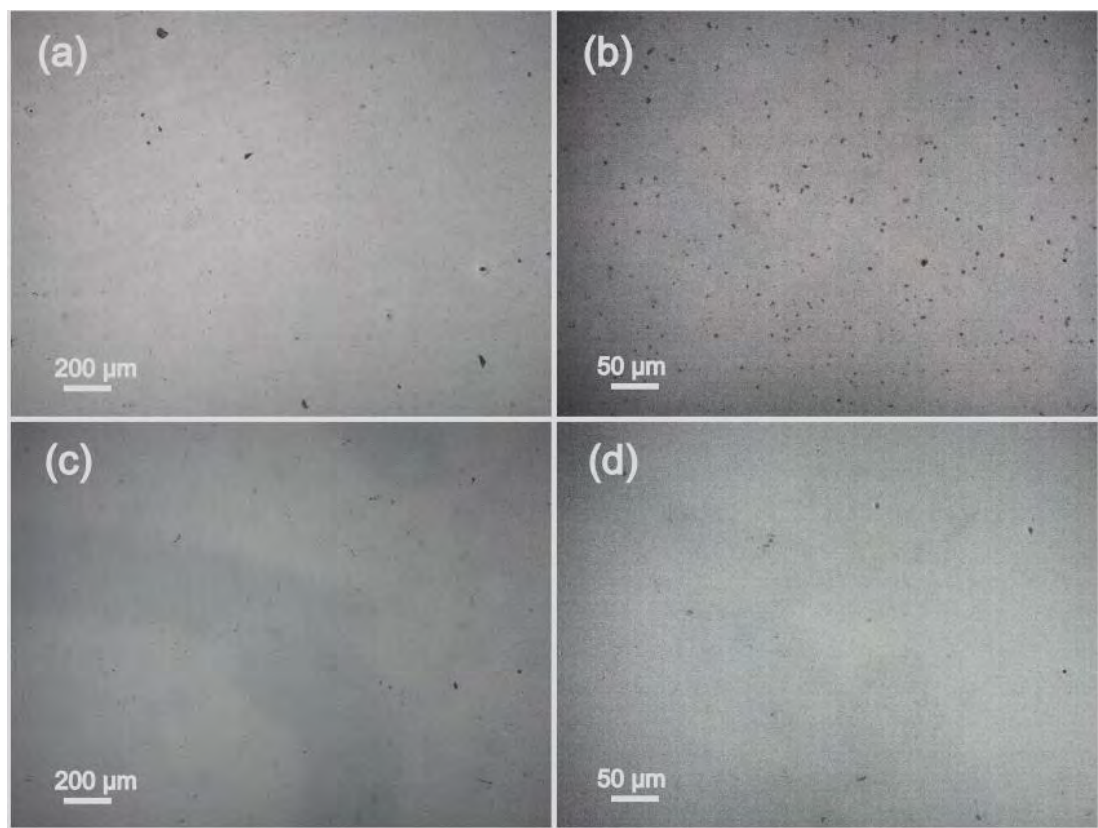


Fig. 4.20. Optical micrographs of films deposited using (a, b) unfiltered solution and (c, d) filtered solution

- b) The problem with the shorted electrodes were clear – some of the sputtered gold reached the bottom FTO layer via a porosity, pinhole, crack or crevice. Only one such defect, if present inside the area covered by the top electrode, is enough to short out the

connection and make electrical measurements of the film impossible. But as it turned out, shorting was only the beginning of the problem. Even the electrodes that were not shorted gave resistivity values differing by up to two or three orders of magnitude. Clearly such a variation cannot be an inherent quality of the film even if some thickness non-uniformity is accounted for. The culprit was identified to be the presence of innumerable dust, dirt or other particulate matter in the film. Fig. 4.20(a, b) shows representative images of a film after annealing. The extremely high amount of visible particulate matter explains why the electrical measurements would not give reliable values. Compared to the size of these particulate matter the thickness of the films were small. These large sized particulate matter, if sampled under a sputtered electrode, would severely contract the effective thickness of the film at its residing place and decrease the resistance value measured using that electrode. We have theorized that the wide variation in resistivity that we have observed is because not all particulate matter will compromise the thickness of the film to the same extent. In order to narrow down the source of these particulate matter, we deposited films using filtered solutions. Fig. 4.20(c, d) shows typical micrographs of films made with filtered solutions. Filtering seemed to have a large positive effect in that the abundance of particulate matter was drastically reduced. Especially in reducing the smaller particulate matter, the effectiveness of filtration was dramatic (compare Fig. 4.20(b) with 4.20(d)). But still, larger particles were present in the films. Hence these particles were not sourced from the solution but rather from the environment during processing of the films. Apparently, the usual amount of dust/particulate matter present in the air in the laboratory was enough to cause significant degradation of quality of our films. If the processing of the films could be done inside a glove box or clean room, better results may have been obtained.

4.3.2 Planar electrode configuration

In this configuration some value of the resistivity could be obtained but they were not reliable. Current seemed to vary randomly at a constant voltage level, and ramping the voltage did not yield a linear increase in current. The reason behind not getting reliable resistivity values was not clear. It might be the case that, some currents flow through the surface of the glass that is beside each side of the film (see Fig. 3.3(b)). This surface current may be due to adsorbed moisture on the glass. An observation to support this situation is that, when the bare glass beside the film is touched by something conducting, like Al foil, the current flowing between the electrodes go up. Since there is no direct connection between the external object touching the glass and the electrodes, there has to be a significant current flowing through the surface of the bare glass itself, which then changes when the glass comes into contact with the external object.

4.3.3 Four-point probe measurement

Somewhat reliable values of resistivity were obtained using this setup, although there were some variation of the resistivity depending on where the probes were placed. Resistivity values between $2 \times 10^5 \Omega \cdot \text{cm}$ to $12 \times 10^5 \Omega \cdot \text{cm}$ were obtained. These values are definitely higher than what would be desired for a ferroelectric BFO film. A way to evaluate whether these values truly represented the resistivity of the films would be to test films differing only in their thickness. Similar resistivity values obtained from films of differing thicknesses would lend much credence to the measurements. Unfortunately, we could not do such tests due to time and resource constraints.

4.4 Magnetic Properties:

Fig. 4.21 shows the raw M-H curve of a few typical samples as well as the empty sample holder. Glass being diamagnetic, the glass holder shows a linear M-H curve with negative

slope. There is another very small contribution in this curve as apparent from the region of the curve near $H = 0$. It is possible that this contribution comes from magnetic impurities sticking

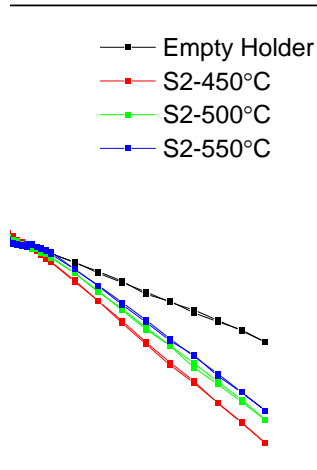


Fig. 4.21. Raw M-H curves of empty sample holder and S2 annealed at 450° C, 500° C and 550° C

to the glass rod that were not removed even after careful cleaning. Subsequent measurements were made using this same rod so that this extraneous contribution, common to all samples, could be subtracted from the obtained data. The raw M-H curves of the samples show a stronger diamagnetic component than the empty glass holder, obviously because of the glass substrate. The very thin film combined with BFO's weak ferromagnetism results in a very small contribution of the film to the overall magnetization. Thus it is imperative to separate from the film's magnetization, the contributions due to the glass holder and the substrate.

The overall magnetic moment detected in the VSM can be written as the sum of three component –

$$M_T = M_{GH} + M_S + M_{TF} = M_{GH} + m_s \chi_G H + M_{TF} \quad (4.1)$$

where, M_T = total magnetic moment, M_{GH} = magnetic moment of the glass holder, M_S = magnetic moment of the substrate, M_{TF} = magnetic moment of the thin film, m_s = mass of the

substrate in g, H = applied field in Oe and χ_G = mass susceptibility of glass substrate in cm^3/g .

All magnetic moments are in emu. In order to determine χ_G , we tested an empty glass substrate of known cross-sectional area and mass. From this data the holder's contribution was subtracted and we obtained a straight line of negative slope belonging to the glass substrate. Its slope was divided by the mass of the substrate to get χ_G .

To extract only M_{TF} , first the raw signal obtained from the empty holder was subtracted from each data set. Then we determined M_S from the susceptibility and mass of sample in each case, which is basically equal to the mass of the substrate since the thin film has negligible weight. Subtraction of M_S gave us only the film's magnetic moment which was converted to emu/cm^3 , wherein the volume of a film was calculated from the thickness of each film and the surface area of the substrate. Because the substrates were not of a regular shape, we approximated its area by comparing its mass to that of another substrate of known area.

Extracted magnetization of the films are shown in Fig. 4.22. The first observation is that, none of the samples show any obvious hysteresis loop which is consistent with the weak ferromagnetic nature of BFO. Increase in annealing temperature seemed to have a positive effect in developing a ferromagnetic characteristic. We concluded from the XRD patterns that full BFO formation does not occur at the lower annealing temperatures (especially 450° C),

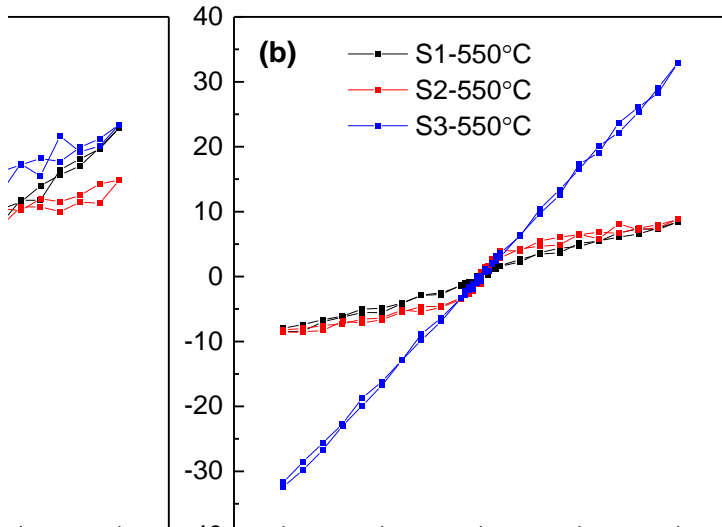


Fig. 4.22. Extracted M-H curves of films

hence the more ferromagnet-like curve observed for the film annealed at 550° C might be related to proper phase formation. On the other hand, Bi excess seems to have a large hand in increasing the magnetization as Fig. 4.22(b) shows. S3's susceptibility was remarkably larger than S1 or S2's. Enhancement of susceptibility indicates a greater ease with which the magnetic moments may align with the external applied field. Fe vacancies, which we argued (in section 4.2.5) to be abundant in S3, could be responsible for this increase. As we have discussed previously, the magnetization due to canting of spins cannot be observed in BFO because of the spin cycloid. But, Fe vacancies would perturb this magnetic superstructure and some latent magnetization might get released. Also, the magnetic moment of an Fe^{3+} adjacent to a V_{Fe} would experience one less exchange interaction than those in a normal lattice site, making the magnetic moment somewhat relaxed and more amenable to aligning with the external field.

4.5 Optical Properties:

Optical absorption characteristics of the films were measured using UV-Vis spectroscopy. The obtained transmission ($\%T$) spectra was converted first to absorbance (A) using the formula,

$$A = \log\left(\frac{100}{\%T}\right) \quad (4.2)$$

and then to absorption coefficient (α) using

$$\alpha = \frac{2.303A}{t} \quad (4.3)$$

where t = thickness of the film in centimeters. Fig. 4.23 depicts the absorbance characteristics of some films synthesized using different parameters. The stoichiometrically varied films showed very similar absorption properties (Fig. 4.23(b)) while films annealed at different temperatures (Fig. 4.23(a)) had some differences. The film annealed at 500° C was mostly similar at longer wavelengths to the one annealed at 550° C but varied at lower frequencies. Especially altered was the absorption of the film annealed at 450° C, which is understandable since this film had a significant amount of phases other than BFO, phases which certainly have their own absorption characteristics.

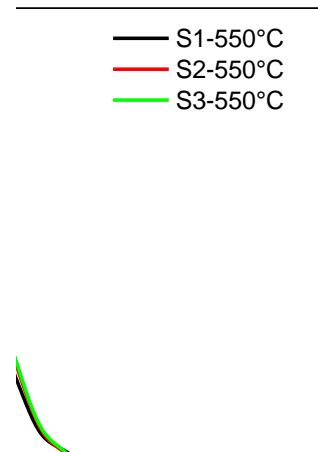


Fig. 4.23. Optical absorbance of the thin films

In order to determine the band-gap we employed Tauc's method [106], assuming a direct band-gap. According to the equation,

$$(\alpha h\nu) = A' (E - E_g)^n \quad (4.4)$$

where A' is a constant, E is the photon energy, E_g is the band gap energy, α is absorption coefficient and n is the power factor of the optical transition mode in a semiconductor, i.e., direct transition ($n=1/2$) or indirect transition ($n=2$), the linear portion of $(\alpha.h\nu)^2$ vs. $h\nu$ plot extrapolated to $y=0$, intercepts the x-axis at the band-gap energy. Fig. 4.24 shows these plots and also the linear extrapolations only for 550° C annealed films. In all three cases, the band-gap is around 2.73 eV which matches well with that of the literature value for BFO thin films [107]. Since the other two cases had the presence of multiple phases a single band-gap would be meaningless for them, and thus their Tauc plots were not drawn.

Fig. 4.24. $(\alpha.h\nu)^2$ vs. $h\nu$ plots for S1, S2 and S3 annealed at 550° C

The relative insensitivity of the band-gap to Bi stoichiometry is understandable since no new elements have been introduced. In essence, the band gap depends on the position of the valence band maximum (VBM) and conduction band minimum (CBM) [22], which consist of different orbitals of the constituent atoms. Since the atomic constituents remain unchanged, the energy of the orbitals making up VBM and CBM also remain mostly unaltered. Of course, some minor changes in the absorption characteristics do occur, and the variation of lattice parameters may also have a role to play.

CONCLUSIONS

The primary focus of this thesis was to produce good quality BFO thin films using cost effective raw materials and simple sol-gel/spin coating processing route. To minimize the costs, we have used metal nitrates instead of the more expensive metal alkoxides and have employed acetic acid instead of acetic anhydride as chelating agent. Although some limitations were faced, we believe our goal has been largely achieved in that we have managed to tune the processing parameters and fabricate dense, well crystallized films with very good phase purity. Our findings can be summarized as follows:

- a) The method of solution dispensation is very important in producing films with maximal coverage of the substrate. We have found that spreading the liquid solution manually after dispensation on to the substrate yielded the best results.
- b) Preheating of substrates is an essential step in producing smooth, continuous films. It was found that film topography and continuity could be controlled by utilizing different substrate preheat temperatures. A preheat temperature of 70° C was enough for smooth film formation while lower temperatures induced progressively rougher and more discontinuous films. On the other hand, preheat temperature did not have any effect on phase formation.
- c) The ratio of 2-methoxyethanol to acetic acid was found to be of lesser significance. A higher proportion of 2-methoxyethanol did seem to produce denser films, but only slightly. Phase formation was unaffected by the solvent ratio.
- d) For satisfactory formation of the perovskite phase and suppression of parasitic phases, 550° C was deemed the most suitable annealing temperature. Lower temperatures produced phase mixtures and/or underdeveloped microstructure whereas the glass substrate could not tolerate higher temperatures.

- e) Surprisingly, our chosen processing route and starting chemistry was proven to be quite effective in producing phase pure BFO, even in case of intentional Bi non-stoichiometry. 5% Bi-deficient and Bi-excess films displayed similar phase purity and microstructure compared to the stoichiometric film.
- f) Rapid heating was identified to be one way of inducing $(100)_{pc}$ texture in the films albeit at the cost of introducing parasitic phases. However, when rapid heating was done in the presence of a pre-annealed BFO seed layer, texture became more pronounced and parasitic phases were found to vanish.
- g) Electrical properties could not be measured in a reliable manner, primarily because of the presence of dust and/or extraneous particles present in the films. Filtration of the solution reduced the number of particles greatly but still it was not enough to make reliable electrical measurements possible.
- h) Magnetization measurements confirmed the weak-ferromagnetic nature of the films. Bi-excess seemed to have a beneficial effect on the magnetization, arguably because of Fe^{3+} vacancies.
- i) Band-gap of the films were determined to be around 2.73 eV and was found to be insensitive to Bi non-stoichiometry.

SUGGESTIONS FOR FUTURE WORK

- a) Analyzing the influence of a greater range of heating rates and/or temperatures on texture development could be carried out.
- b) Inducing higher degrees of texture should be attempted. Making a thinner seed layer and depositing a greater number of subsequent layers on top should bring about better columnar grain structure and texture.
- c) Making the seed layer discontinuous by keeping the preheat temperature low, could also help in creating films that are more textured.
- d) Effect of metal nitrate concentration on the film properties could be evaluated. Possibility of controlling film microstructure, grain size, thickness and smoothness through variation of solution concentration seems rational.
- e) Microporosity/void removal could be attempted by tuning the solution chemistry further, for example by optimizing the solvent ratio and/or metal nitrate concentration.
- f) Films should be made inside a glove box or clean room in an attempt to obtain films of sufficient quality that would make electrical (especially ferroelectric) measurements possible.
- g) Film with thickness lower than 64 nm (i.e. smaller than the spin cycloid length) could be fabricated to evaluate any possible improvement in magnetization.
- h) Fabricating films doped with various elements in order to enhance the various properties.
- i) Photocatalytic ability of pure and doped BFO films should be assessed. The effect of film roughness/discontinuity, induced by low preheat temperatures, on the photocatalytic activity should be studied.

BIBLIOGRAPHY

- [1]. N.A. Spaldin, S.-W. Cheong, and R. Ramesh, *Multiferroics: past, present, and future*. Phys. Today, 2010. **63**(10): p. 38-43.
- [2]. G. Catalan and J.F. Scott, *Physics and applications of bismuth ferrite*. Advanced Materials, 2009. **21**(24): p. 2463-2485.
- [3]. I. Sosnowska, T.P. Neumaier, and E. Steichele, *Spiral magnetic ordering in bismuth ferrite*. Journal of Physics C: Solid State Physics, 1982. **15**(23): p. 4835.
- [4]. G. Smolenskiĭ and I. Chupis, *Ferroelectromagnets*. Soviet Physics Uspekhi, 1982. **25**(7): p. 475.
- [5]. S. Ghosh, S. Dasgupta, A. Sen, and H. Sekhar Maiti, *Low-temperature synthesis of nanosized bismuth ferrite by soft chemical route*. Journal of the American Ceramic Society, 2005. **88**(5): p. 1349-1352.
- [6]. Z.X. Cheng, et al., *Structure, ferroelectric properties, and magnetic properties of the La-doped bismuth ferrite*. Journal of Applied Physics, 2008. **103**(7): p. 07E507.
- [7]. S. Gupta, M. Tomar, and V. Gupta, *Ferroelectric photovoltaic response to structural transformations in doped BiFeO₃ derivative thin films*. Materials & Design, 2016. **105**: p. 296-300.
- [8]. R. Ramesh and N.A. Spaldin, *Multiferroics: progress and prospects in thin films*. Nature materials, 2007. **6**(1): p. 21-29.
- [9]. C.-H. Yang, et al., *Electric modulation of conduction in multiferroic Ca-doped BiFeO₃ films*. Nature materials, 2009. **8**(6): p. 485-493.
- [10]. J. Wang, et al., *Epitaxial BiFeO₃ multiferroic thin film heterostructures*. Science, 2003. **299**(5613): p. 1719-1722.
- [11]. R. Nechache, C. Harnagea, S. Li, L. Cardenas, W. Huang, J. Chakrabartty, and F. Rosei, *Bandgap tuning of multiferroic oxide solar cells*. Nature Photonics, 2015. **9**(1): p. 61.
- [12]. M. Qin, K. Yao, and Y.C. Liang, *Photovoltaic characteristics in polycrystalline and epitaxial (Pb 0.97 La 0.03)(Zr 0.52 Ti 0.48) O₃ ferroelectric thin films sandwiched between different top and bottom electrodes*. Journal of applied physics, 2009. **105**(6): p. 061624.
- [13]. R.W. Schwartz, *Chemical solution deposition of perovskite thin films*. Chemistry of Materials, 1997. **9**(11): p. 2325-2340.
- [14]. L. Zhang, J. Chen, J. Cao, D. He, and X. Xing, *Large resistive switching and switchable photovoltaic response in ferroelectric doped BiFeO₃-based thin films by chemical solution deposition*. Journal of Materials Chemistry C, 2015. **3**(18): p. 4706-4712.

- [15]. Q. Zhang, N. Valanoor, and O. Standard, *Epitaxial (001) BiFeO₃ thin-films with excellent ferroelectric properties by chemical solution deposition-the role of gelation.* Journal of Materials Chemistry C, 2015. **3**(3): p. 582-595.
- [16]. Y. Liu, J. Wei, Y. Guo, T. Yang, and Z. Xu, *Phase transition, interband electronic transitions and enhanced ferroelectric properties in Mn and Sm co-doped bismuth ferrite films.* RSC Advances, 2016. **6**(99): p. 96563-96572.
- [17]. S. Mukherjee, R. Gupta, A. Garg, V. Bansal, and S. Bhargava, *Influence of Zr doping on the structure and ferroelectric properties of BiFeO₃ thin films.* Journal of Applied Physics, 2010. **107**(12): p. 123535.
- [18]. L.E. Cross, *Ferroic materials and composites: past, present and future,* in *Advanced Ceramics III.* 1990, Springer. p. 71-102.
- [19]. A. Zenkevich, Y. Matveyev, K. Maksimova, R. Gaynudinov, A. Tolstikhina, and V. Fridkin, *Giant bulk photovoltaic effect in thin ferroelectric BaTiO₃ films.* Physical Review B, 2014. **90**(16): p. 161409.
- [20]. J.M. Yeomans, *Statistical mechanics of phase transitions.* 1992: Clarendon Press.
- [21]. M.E. Lines and A.M. Glass, *Principles and applications of ferroelectrics and related materials.* 1977: Oxford university press.
- [22]. C. Kittel, P. McEuen, and P. McEuen, *Introduction to solid state physics.* Vol. 8. 1996: Wiley New York.
- [23]. B.D. Cullity and C.D. Graham, *Introduction to magnetic materials.* 2011: John Wiley & Sons.
- [24]. E. Salje, *Phase transitions in ferroelastic and co-elastic crystals.* Ferroelectrics, 1990. **104**(1): p. 111-120.
- [25]. W. Eerenstein, N. Mathur, and J.F. Scott, *Multiferroic and magnetoelectric materials.* nature, 2006. **442**(7104): p. 759.
- [26]. D.I. Khomskii, *Multiferroics: Different ways to combine magnetism and ferroelectricity.* Journal of Magnetism and Magnetic Materials, 2006. **306**(1): p. 1-8.
- [27]. S.-W. Cheong and M. Mostovoy, *Multiferroics: a magnetic twist for ferroelectricity.* Nature materials, 2007. **6**(1): p. 13.
- [28]. M. Fiebig, *Revival of the magnetoelectric effect.* Journal of Physics D: Applied Physics, 2005. **38**(8): p. R123.
- [29]. P. Curie, *Sur la symétrie dans les phénomènes physiques, symétrie d'un champ électrique et d'un champ magnétique.* J. Phys. Theor. Appl., 1894. **3**(1): p. 393-415.
- [30]. J. Valasek, *Piezo-electric and allied phenomena in Rochelle salt.* Physical review, 1921. **17**(4): p. 475.
- [31]. T. O'dell, *The electrodynamics of magneto-electric media.* Philosophical Magazine, 1962. **7**(82): p. 1653-1669.

- [32]. I. Dzyaloshinskii, *Topological model of a heisenberg spin glass*. JETP Letters, 1959. **37**: p. 881-882.
- [33]. D. Astrov, *The magnetoelectric effect in antiferromagnetics*. Sov. Phys. JETP, 1960. **11**(3): p. 708-709.
- [34]. E. Ascher, H. Rieder, H. Schmid, and H. Stössel, *Some Properties of Ferromagnetoelectric Nickel-Iodine Boracite, Ni₃B₇O₁₃I*. Journal of Applied Physics, 1966. **37**(3): p. 1404-1405.
- [35]. H. Schmid, *Multi-ferroic magnetoelectrics*. Ferroelectrics, 1994. **162**(1): p. 317-338.
- [36]. F. Kubel and H. Schmid, *Structure of a ferroelectric and ferroelastic monodomain crystal of the perovskite BiFeO₃*. Acta crystallographica section B, 1990. **46**(6): p. 698-702.
- [37]. A. Palewicz, I. Sosnowska, R. Przenioslo, and A. Hewat, *BiFeO₃ crystal structure at low temperatures*. Acta Physica Polonica-Series A General Physics, 2010. **117**(2): p. 296.
- [38]. R.t. Shannon, *Revised effective ionic radii and systematic studies of interatomic distances in halides and chalcogenides*. Acta Crystallographica Section A: Crystal Physics, Diffraction, Theoretical and General Crystallography, 1976. **32**(5): p. 751-767.
- [39]. R. Palai, et al., *β phase and $\gamma - \beta$ metal-insulator transition in multiferroic Bi Fe O 3*. Physical Review B, 2008. **77**(1): p. 014110.
- [40]. M. Polomska, W. Kaczmarek, and Z. Pajak, *Electric and magnetic properties of (B1-xLax) FeO₃ solid solutions*. physica status solidi (a), 1974. **23**(2): p. 567-574.
- [41]. I.A. Kornev, S. Lisenkov, R. Haumont, B. Dkhil, and L. Bellaiche, *Finite-temperature properties of multiferroic BiFeO 3*. Physical Review Letters, 2007. **99**(22): p. 227602.
- [42]. R. Haumont, I.A. Kornev, S. Lisenkov, L. Bellaiche, J. Kreisel, and B. Dkhil, *Phase stability and structural temperature dependence in powdered multiferroic BiFeO 3*. Physical review B, 2008. **78**(13): p. 134108.
- [43]. S.M. Selbach, T. Tybell, M.-A. Einarsrud, and T. Grande, *High-temperature semiconducting cubic phase of BiFe 0.7 Mn 0.3 O 3+ δ*. Physical Review B, 2009. **79**(21): p. 214113.
- [44]. F. Zavaliche, R. Das, D. Kim, C. Eom, S. Yang, P. Shafer, and R. Ramesh, *Ferroelectric domain structure in epitaxial Bi Fe O 3 films*. Applied Physics Letters, 2005. **87**(18): p. 182912.
- [45]. J.R. Teague, R. Gerson, and W.J. James, *Dielectric hysteresis in single crystal BiFeO₃*. Solid State Communications, 1970. **8**(13): p. 1073-1074.
- [46]. P.W. Anderson, *New approach to the theory of superexchange interactions*. Physical Review, 1959. **115**(1): p. 2.

- [47]. I.A. Sergienko and E. Dagotto, *Role of the Dzyaloshinskii-Moriya interaction in multiferroic perovskites*. Physical Review B, 2006. **73**(9): p. 094434.
- [48]. D. Lebeugle, D. Colson, A. Forget, M. Viret, A. Bataille, and A. Gukasov, *Electric-field-induced spin flop in BiFeO₃ single crystals at room temperature*. Physical review letters, 2008. **100**(22): p. 227602.
- [49]. P. Fischer, M. Polomska, I. Sosnowska, and M. Szymanski, *Temperature dependence of the crystal and magnetic structures of BiFeO₃*. Journal of Physics C: Solid State Physics, 1980. **13**(10): p. 1931.
- [50]. J. Li, et al., *Dramatically enhanced polarization in (001), (101), and (111) BiFeO₃ thin films due to epitaxial-induced transitions*. Applied physics letters, 2004. **84**(25): p. 5261-5263.
- [51]. H. Béa, et al., *Crystallographic, magnetic, and ferroelectric structures of bulklike Bi Fe O₃ thin films*. Applied Physics Letters, 2008. **93**(7): p. 072901.
- [52]. R. Das, et al., *Synthesis and ferroelectric properties of epitaxial Bi Fe O₃ thin films grown by sputtering*. Applied physics letters, 2006. **88**(24): p. 242904.
- [53]. H. Jang, et al., *Epitaxial (001) Bi Fe O₃ membranes with substantially reduced fatigue and leakage*. Applied Physics Letters, 2008. **92**(6): p. 062910.
- [54]. X. Lou, C. Yang, T. Tang, Y. Lin, M. Zhang, and J. Scott, *Formation of magnetite in bismuth ferrite under voltage stressing*. Applied physics letters, 2007. **90**(26): p. 262908.
- [55]. D.I. Woodward, I.M. Reaney, R.E. Eitel, and C.A. Randall, *Crystal and domain structure of the BiFeO₃-PbTiO₃ solid solution*. Journal of applied physics, 2003. **94**(5): p. 3313-3318.
- [56]. B. Noheda, D. Cox, G. Shirane, J. Gonzalo, L. Cross, and S. Park, *A monoclinic ferroelectric phase in the Pb (Zr 1-x Ti x) O₃ solid solution*. Applied physics letters, 1999. **74**(14): p. 2059-2061.
- [57]. H. Béa, M. Gajek, M. Bibes, and A. Barthélémy, *Spintronics with multiferroics*. Journal of Physics: Condensed Matter, 2008. **20**(43): p. 434221.
- [58]. T. Zhao, et al., *Electrical control of antiferromagnetic domains in multiferroic BiFeO₃ films at room temperature*. Nature materials, 2006. **5**(10): p. 823.
- [59]. S. Lee, W. Ratcliff, S. Cheong, and V. Kiryukhin, *Electric field control of the magnetic state in Bi Fe O₃ single crystals*. Applied Physics Letters, 2008. **92**(19): p. 192906.
- [60]. H. Béa, et al., *Mechanisms of exchange bias with multiferroic BiFeO₃ epitaxial thin films*. Physical review letters, 2008. **100**(1): p. 017204.
- [61]. H. Béa, et al., *Ferroelectricity down to at least 2 nm in multiferroic BiFeO₃ epitaxial thin films*. Japanese journal of applied physics, 2006. **45**(2L): p. L187.

- [62]. T. Choi, S. Lee, Y. Choi, V. Kiryukhin, and S.-W. Cheong, *Switchable ferroelectric diode and photovoltaic effect in BiFeO₃*. Science, 2009. **324**(5923): p. 63-66.
- [63]. A. Glass, D.v.d. Linde, and T. Negran, *High-voltage bulk photovoltaic effect and the photorefractive process in LiNbO₃*, in *Landmark Papers On Photorefractive Nonlinear Optics*. 1995, World Scientific. p. 371-373.
- [64]. P.S. Brody and F. Crowne, *Mechanism for the high voltage photovoltaic effect in ceramic ferroelectrics*. Journal of Electronic Materials, 1975. **4**(5): p. 955-971.
- [65]. S. Yang, et al., *Above-bandgap voltages from ferroelectric photovoltaic devices*. Nature nanotechnology, 2010. **5**(2): p. 143.
- [66]. D. Huang, H. Deng, P. Yang, and J. Chu, *Optical and electrical properties of multiferroic bismuth ferrite thin films fabricated by sol-gel technique*. Materials Letters, 2010. **64**(20): p. 2233-2235.
- [67]. N. Dix, et al., *On the strain coupling across vertical interfaces of switchable BiFeO₃-CoFe₂O₄ multiferroic nanostructures*. Applied Physics Letters, 2009. **95**(6): p. 062907.
- [68]. C. Wang, X. Liu, S. Sheng, Y. Zhou, H. Liu, and Y. Sun, *Photovoltaic mechanism in Na-substituted BiFeO₃ films*. Journal of Physics D: Applied Physics, 2014. **47**(35): p. 355104.
- [69]. S. Gupta, M. Tomar, and V. Gupta, *Ferroelectric photovoltaic properties of Ce and Mn codoped BiFeO₃ thin film*. Journal of Applied Physics, 2014. **115**(1): p. 014102.
- [70]. V.M. Fridkin, *Photoferroelectrics*. Vol. 9. 2012: Springer Science & Business Media.
- [71]. P.S. Brody, *Semiconductor-ferroelectric nonvolatile memory using anomalous high photovoltages in ferroelectric ceramics*. Applied Physics Letters, 1981. **38**(3): p. 153-155.
- [72]. M. Ichiki, Y. Morikawa, Y. Mabune, and T. Nakada, *Electrical properties of photovoltaic lead lanthanum zirconate titanate in an electrostatic-optical motor application*. Journal of the European Ceramic Society, 2004. **24**(6): p. 1709-1714.
- [73]. Z. Fan, K. Yao, and J. Wang, *Photovoltaic effect in an indium-tin-oxide/ZnO/BiFeO₃/Pt heterostructure*. Applied Physics Letters, 2014. **105**(16): p. 162903.
- [74]. S.M. Young, F. Zheng, and A.M. Rappe, *First-principles calculation of the bulk photovoltaic effect in bismuth ferrite*. Physical review letters, 2012. **109**(23): p. 236601.
- [75]. W. Ji, K. Yao, and Y.C. Liang, *Evidence of bulk photovoltaic effect and large tensor coefficient in ferroelectric BiFeO₃ thin films*. Physical Review B, 2011. **84**(9): p. 094115.

- [76]. F. Tyholdt, S. Jørgensen, H. Fjellvåg, and A. Gunnaes, *Synthesis of oriented BiFeO₃ thin films by chemical solution deposition: phase, texture, and microstructural development*. Journal of materials research, 2005. **20**(8): p. 2127-2139.
- [77]. X. Qi, J. Dho, R. Tomov, M.G. Blamire, and J.L. MacManus-Driscoll, *Greatly reduced leakage current and conduction mechanism in aliovalent-ion-doped BiFeO₃*. Applied Physics Letters, 2005. **86**(6).
- [78]. S. Iakovlev, C.-H. Solterbeck, M. Kuhnke, and M. Es-Souni, *Multiferroic BiFeO₃ thin films processed via chemical solution deposition: Structural and electrical characterization*. Journal of applied physics, 2005. **97**(9): p. 094901.
- [79]. M. Valant, A.-K. Axelsson, and N. Alford, *Peculiarities of a solid-state synthesis of multiferroic polycrystalline BiFeO₃*. Chemistry of Materials, 2007. **19**(22): p. 5431-5436.
- [80]. C.J. Brinker and G.W. Scherer, *Sol-gel science: the physics and chemistry of sol-gel processing*. 2013: Academic press.
- [81]. R. Ueno, S. Okaura, H. Funakubo, and K. Saito, *Crystal structure and electrical properties of epitaxial BiFeO₃ thin films grown by metal organic chemical vapor deposition*. Japanese journal of applied physics, 2005. **44**(9L): p. L1231.
- [82]. S.K. Singh, R. Ueno, H. Funakubo, H. Uchida, S. Koda, and H. Ishiwara, *Dependence of ferroelectric properties on thickness of BiFeO₃ thin films fabricated by chemical solution deposition*. Japanese journal of applied physics, 2005. **44**(12R): p. 8525.
- [83]. S.K. Singh and H. Ishiwara, *Reduced leakage current in BiFeO₃ thin films on Si substrates formed by a chemical solution method*. Japanese journal of applied physics, 2005. **44**(5L): p. L734.
- [84]. F. Tyholdt, H. Fjellvåg, A.E. Gunnæs, and A. Olsen, *Synthesis of epitaxial BiFeO₃ films by chemical solution deposition on Pt (100)*. Journal of Applied Physics, 2007. **102**(7): p. 074108.
- [85]. Y. Nakamura, S. Nakashima, and M. Okuyama, *Improvement of ferroelectric properties of BiFeO₃ thin films by postmetallization annealing and electric field application*. Journal of Applied Physics, 2009. **105**(6): p. 061616.
- [86]. Y. Nakamura, K.-Y. Yun, S. Nakashima, and M. Okuyama, *Sol-gel preparation and characterization of multiferroic BiFeO₃ thin films with various Bi/Fe ratio*. Integrated Ferroelectrics, 2007. **95**(1): p. 226-233.
- [87]. C.D. Chandler, C. Roger, and M.J. Hampden-Smith, *Chemical aspects of solution routes to perovskite-phase mixed-metal oxides from metal-organic precursors*. Chemical reviews, 1993. **93**(3): p. 1205-1241.
- [88]. J. West and L. Hench, *The sol-gel process*. Chem. Rev, 1990. **90**: p. 33-72.

- [89]. C. Yu, M. Kao, H. Chen, S. Young, and C. Lin, *Electrical Properties and Leakage Current Mechanisms of Bi 3.2 Gd 0.8 Ti 3 O 12 Thin Films Prepared by a Sol-Gel Method*. Journal of superconductivity and novel magnetism, 2010. **23**(6): p. 929-932.
- [90]. Y. Zhang, S. Yu, and J. Cheng, *The study of Bi_xCr_yFe_{1-x}O₃ thin films synthesized by sol-gel technique*. Journal of the European Ceramic Society, 2010. **30**(2): p. 271-275.
- [91]. F.P. Lai, J.F. Li, and W. Gong. *Preparation of Ferroelectric K0.5Na0.5NbO3 Films by Sol-Gel Processing*. in *Key Engineering Materials*. 2007. Trans Tech Publ.
- [92]. J.H. Xu, H. Ke, D.C. Jia, W. Wang, and Y. Zhou. *Preparation of BiFeO3 Nanopowders Using Acetylacetone as Stabilizer*. in *Key Engineering Materials*. 2010. Trans Tech Publ.
- [93]. F. Gao, et al., *Visible-light photocatalytic properties of weak magnetic BiFeO3 nanoparticles*. Advanced Materials, 2007. **19**(19): p. 2889-2892.
- [94]. R. Guo, L. Fang, W. Dong, F. Zheng, and M. Shen, *Enhanced photocatalytic activity and ferromagnetism in Gd doped BiFeO3 nanoparticles*. The Journal of Physical Chemistry C, 2010. **114**(49): p. 21390-21396.
- [95]. F. Gao, Y. Yuan, K. Wang, X. Chen, F. Chen, J.-M. Liu, and Z. Ren, *Preparation and photoabsorption characterization of Bi Fe O 3 nanowires*. Applied Physics Letters, 2006. **89**(10): p. 102506.
- [96]. C. Thompson and R. Carel. *Grain growth and texture evolution in thin films*. in *Materials Science Forum*. 1996. Trans Tech Publ.
- [97]. M.B. González, A. Wu, and P.M. Vilarinho, *Influence of Solvents on the Microstructure and dielectric properties of Ba0.5Sr0.5TiO3 thin films prepared by a diol-based sol-gel process*. Chemistry of materials, 2006. **18**(7): p. 1737-1744.
- [98]. H. Frost, *Microstructural evolution in thin films*. Materials characterization, 1994. **32**(4): p. 257-273.
- [99]. C. Gutiérrez-Lázaro, et al., *Solution Synthesis of BiFeO 3 Thin Films onto Silicon Substrates with Ferroelectric, Magnetic, and Optical Functionalities*. Journal of the American Ceramic Society, 2013. **96**(10): p. 3061-3069.
- [100]. K.Y. Yun, M. Noda, and M. Okuyama, *Effects of annealing atmosphere on crystallization and electrical properties in BiFeO 3 thin films by chemical solution deposition (CSD)*. Journal of the Korean Physical Society, 2003. **42**(Suppl.): p. 1153-1156.
- [101]. X. Tang, X. Zhu, J. Dai, and Y. Sun, *Self-limited grain growth, dielectric, leakage and ferroelectric properties of nanocrystalline BiFeO3 thin films by chemical solution deposition*. Acta Materialia, 2013. **61**(5): p. 1739-1747.

- [102]. I. Miccoli, F. Edler, H. Pfnür, and C. Tegenkamp, *The 100th anniversary of the four-point probe technique: the role of probe geometries in isotropic and anisotropic systems*. Journal of Physics: Condensed Matter, 2015. **27**(22): p. 223201.
- [103]. K. Ahadi, S. Mahdavi, A. Nemati, and M. Kianinia, *Photoconductivity and diode effect in Bi rich multiferroic BiFeO₃ thin films grown by pulsed-laser deposition*. Journal of Materials Science: Materials in Electronics, 2011. **22**(7): p. 815-820.
- [104]. A.E. Paladino and W. Kingery, *Aluminum ion diffusion in aluminum oxide*. The Journal of Chemical Physics, 1962. **37**(5): p. 957-962.
- [105]. N. Bassiri-Gharb, Y. Bastani, and A. Bernal, *Chemical solution growth of ferroelectric oxide thin films and nanostructures*. Chemical Society Reviews, 2014. **43**(7): p. 2125-2140.
- [106]. J. Tauc, R. Grigorovici, and A. Vancu, *Optical properties and electronic structure of amorphous germanium*. physica status solidi (b), 1966. **15**(2): p. 627-637.
- [107]. J.F. Ihlefeld, et al., *Optical band gap of BiFeO₃ grown by molecular-beam epitaxy*. Applied Physics Letters, 2008. **92**(14): p. 142908.